



Computational aerodynamics for soft-wing kite design

Jelle Agatho Wilhelm Poland¹, Kasper Raphaël G Masure¹, Oriol Cayon¹, and Roland Schmehl¹

¹Faculty of Aerospace Engineering, Delft University of Technology, Kluyverweg 1, 2629 HS, Delft, the Netherlands

Correspondence: Jelle Agatho Wilhelm Poland (j.a.w.poland@tudelft.nl)

Abstract. Soft-wing kites are morphing, bridled, tensile lifting surfaces used for wind-assisted ship propulsion and airborne wind energy applications. Their swept-back planform, pronounced anhedral, and unconventional leading-edge geometry induce complex aerodynamic behaviour that challenges conventional modelling approaches. For leading-edge inflatable (LEI) kites, pressure-side separation induced by the inflated tubular leading edge renders classical inviscid methods insufficient, thereby necessitating sectional input from higher-fidelity approaches. This study presents and applies a computationally efficient aerodynamic framework to an LEI kite by coupling a vortex step method (VSM) with RANS-derived airfoil polars validated against wind-tunnel measurements. The RANS simulations were used to train a machine-learning surrogate model to facilitate parametric design studies. Applying machine learning to LEI kite aerodynamics is novel, and it achieves $R^2 > 0.98$ across the considered parameter space. Three-dimensional load predictions for the TU Delft V3 LEI kite were evaluated against wind-tunnel data and reference three-dimensional RANS simulations. Within the operational incidence range $\alpha \in [-1, 10]^\circ$, the predicted lift and drag agree with measurements to within 9% and 13%, respectively. Across this range, the framework reproduces the measured aerodynamic trends more consistently than the reference three-dimensional RANS results, while reducing the computational cost by several orders of magnitude. A rigid-body stability analysis indicated static stability in roll, pitch, and yaw, but limited aerodynamic damping within the quasi-steady model. Parametric analyses revealed inherent trade-offs between aerodynamic efficiency and stability, motivating the adoption of multi-objective optimisation strategies. The validated framework provides high predictive accuracy at low computational cost and forms a foundation for rapid aerodynamic analysis, stability assessment, design optimisation, and aero-structural coupling in the conceptual and preliminary design phases.

1 Introduction

Soft kites have expanded beyond their original use in marine sports to renewable energy applications, most notably airborne wind energy (AWE) and wind-assisted ship propulsion (WASP). A soft kite is a tensile structure consisting of a lightweight membrane wing supported by a bridle line system that transfers the aerodynamic loads and serves as the actuation mechanism (Oehler and Schmehl, 2019). The employed membrane wings can be broadly categorised into three different types: ram-air wings with two stacked membrane layers, connected by membrane ribs and inflated by the incoming flow, leading-edge inflatable (LEI) wings with a pre-inflated tubular frame to which a single membrane layer is attached, and single-skin wings with only one membrane layer. The present study focuses on kites using LEI wings, although the general modelling approach can be applied to other types. LEI kites are morphing aerodynamic control surfaces that deform due to aeroelastic



coupling (Breukels et al., 2013) and in response to a changing geometry of the bridle line system due to actuation input (Hummel et al., 2019; Elfert et al., 2024). By relying on bridle lines as primary load-bearing components, LEI kites, and soft kites in general, can achieve exceptionally high lift-to-weight ratios compared to other flying systems.

30 Design approaches common for sports kites rely heavily on experimental testing to determine the aerodynamic performance. Likewise, within AWE and WASP, control strategies rely on empirical measurements of control responses to inform gain tuning. When scaling kites to sizes required for commercially meaningful wind energy harvesting, such reliance on experiments becomes prohibitively costly, restricting iterative development cycles and increasing risks. Instead, numerical simulation tools can be used effectively to assess kite designs, control responses, and stability derivatives, and to optimise flight paths in a
35 virtual environment, without reliance on extensive prototype testing. But to realise the full potential of these tools, fluid-structure interaction (FSI) phenomena must be accounted for by modelling the two-way coupling between aerodynamic loads and structural deformation (Candade et al., 2020). For modelling FSI phenomena, such aerodynamic models have typically been combined with high-fidelity structural solvers using iterative coupling (Bosch et al., 2014; Lodies et al., 2019; Folkersma et al., 2020; Thedens, 2022). In such partitioned frameworks, the aerodynamic and structural solvers exchange loads and
40 displacements in successive iterations until convergence. These iterative procedures make computational speed a critical factor, particularly in the context of design and optimisation.

Simulating the aerodynamics of soft-wing kites is challenging owing to their complex geometry, characterised by a swept-back planform, low aspect ratio, and pronounced anhedral. A recent review synthesised the state of the art in AWE aerodynamics, spanning prototype architectures and numerical and experimental methods from potential-flow models to high-
45 fidelity Reynolds-averaged Navier–Stokes (RANS) and large-eddy simulation (LES) approaches (Castro-Fernández et al., 2026). Within this context, 2D RANS computational fluid dynamics (CFD) simulations of LEI kites have been conducted to explore variations in Reynolds number, angle of attack, and sideslip angle (Deaves, 2015; Viré et al., 2020, 2022). These studies, performed with k - ω SST turbulence and γ - Re_θ transition models, revealed characteristic separation zones and three-dimensional (3D) crossflow effects typical of curved, low-aspect-ratio wings. Despite providing valuable verification data, the
50 high computational cost of these simulations makes them unsuitable for iterative optimisation.

Lower-fidelity methods have been developed, including lifting-line (LL) and vortex-lattice formulations adapted for curved planforms and low aspect ratios (Gaunaa et al., 2011; Leloup et al., 2013; Branlard et al., 2022; Duport, 2018), as well as nonlinear vortex-lattice and panel-based formulations capable of capturing moderate flow separation (Kappel, 2012; Leuthold, 2015). Panel and vortex-lattice methods fail for LEI kites because they cannot accurately capture flow separation and subse-
55 quent reattachment, which dominate the pressure side of the wing throughout most of its flight envelope (Folkersma et al., 2019). Proposed multiple-wake extension (Leuthold, 2015) partially mitigates this limitation but ultimately suffers from the same underlying problem: when the reattachment line intersects a separation line, the model cannot robustly resolve the local flow topology. Maintaining flow tangency and impermeability in these regions accurately requires prohibitively fine body and wake discretisation, leading to numerical instability and computational costs that undermine the method’s intended efficiency.

60 Taken together, these considerations motivate the use of LL-based formulations as a computationally efficient basis for aerodynamic simulation, as they retain the dominant three-dimensional induction effects while avoiding the prohibitive cost



of high-fidelity CFD. To place the present approach in context, and clarify the assumptions and limitations that matter for soft-wing kites, the following summarises key developments in LL theory over the past century, with emphasis on extensions relevant to robust and efficient aerodynamic modelling.

65 1.1 A century of lifting-line methods

Prandtl (1918) formulated the LL method, providing the first analytical method for predicting lift and induced drag on finite wings by modelling a wing as a bound vortex accompanied by a trailing vortex sheet. Prandtl discretised the wing into spanwise sections and assumed the section lift to be equivalent to that of an infinite wing, enabling the use of the two-dimensional (2D) vortex lifting-law, i.e. the Kutta–Joukowski theorem Kutta (1902). Instead of using the undisturbed free stream velocity, Prandtl
70 used the vector sum of free stream velocity and induced velocity by the trailing vortex sheet.

Subsequent work extended the method’s applicability, thereby establishing LL theory as a practical design tool. Munk (1923) introduced the Stagger Theorem, showing that induced drag is invariant to spanwise shifting of lifting elements, while Glauert (1926) generalised the theory to accommodate non-elliptical spanwise circulation distributions arising from chord variation, twist, camber variation, and other geometric departures from the classical planar wing.

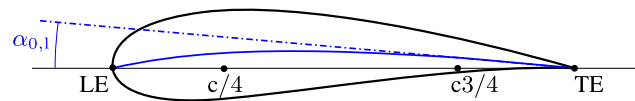


Figure 1. Airfoil illustration indicating the leading-edge (LE), quarter-chord point ($c/4$), three-quarter-chord point ($c3/4$), trailing-edge (TE) and the approximate zero-lift angle of attack ($\alpha_{0,1}$) following Pistolessi (1932).

75 Pistolessi (1932) found that the zero-lift angle of attack of an airfoil can be approximated by the angle of the camber line tangent at the three-quarter chord point, see Fig. 1. This implies that the downwash induced by the entire vortex system should be computed at the three-quarter-chord control point (where the boundary condition is enforced), not at the quarter-chord point where the bound vortex is located. Building on Munk, Glauert, and Pistolessi, Mutterperl (1941) introduced a Fourier-series-based method to determine the spanwise circulation distribution, making it more flexible for non-elliptical wings and
80 able to deal with moderate back-sweep by including the effect of induced velocity by the bound vortex on itself. Weissinger (1947) reformulated Prandtl’s LL method using a finite set of discrete horseshoe vortices. This discrete formulation facilitated numerical implementation and showed improved robustness for swept and forward-swept wings (Weissinger, 1947; van Dorn and DeYoung, 1947).

Tani (1934) is believed to have developed the first successful technique for incorporating nonlinear two-dimensional sectional lift characteristics into the LL formulation, thereby relaxing the classical assumption of a linear sectional lift law with
85 constant lift-curve slope. Most works, however, refer to Sivells and Neely (1947), who documented the method of introducing nonlinearity using airfoil data more accessibly and extensively. Piszkin and Levinsky (1976) subsequently reformulated the Weissinger method by generalising the no-through-flow condition and introducing an iterative procedure to match the sectional circulation with prescribed two-dimensional airfoil polars, referring to this approach as the nonlinear LL method.



90 These developments marked an important conceptual transition in LL modelling. While classical formulations determine circulation by enforcing a no-through-flow condition on the lifting surface, the formulation of Piszkin and Levinsky (1976) and its successors adopts a circulation–matching approach, in which the sectional circulation is adjusted to be consistent with prescribed two-dimensional airfoil polars. This yields a hybrid viscous–inviscid LL formulation that combines inviscid induction modelling with viscous sectional aerodynamics. This formulation enables the inclusion of nonlinear sectional lift
95 polars, e.g., with stall, by relaxing the strict no-through-flow condition of classical potential-flow models.

According to Mukherjee et al. (2003), Piszkin and Levinsky’s nonlinear LL method is a form of a vortex model and more commonly referred to as a single chordwise row vortex lattice method or a discrete-vortex Weissinger method. A similar formulation was implemented in the LINAIR code (Durston, 1993) and used by Brown (1993) to study parafoil control. Barnes (1997) introduced the vortex step method (VSM) as an enhanced LL formulation, combining a Weissinger-type discretisation
100 with a circulation–matching approach based on sectional airfoil data. By recasting the problem in terms of discrete vortex steps and enforcing the flow-tangency condition at the three-quarter-chord control point while retaining the bound vortex near the quarter-chord location, Barnes improved the prediction of induced drag and provided a robust numerical framework for nonlinear LL implementations.

Cone (1962) modelled non-planar wings, i.e., those with a non-zero dihedral or anhedral angle, using conformal transfor-
105 mation and electrical analogue techniques. Phillips and Snyder (2000) recommended aligning the trailing vortex sheet with the undisturbed free stream to maintain consistency with the linearised LL formulation. Allowing the wake direction to depend on the locally induced velocity would introduce geometric nonlinearity and require a free-wake treatment. For strongly swept or highly anhedral configurations, spanwise-varying wake directions may additionally lead to geometric incompatibilities within a straight, semi-infinite filament model, such as filament convergence or intersection.

110 These developments laid the foundation for contemporary discrete-vortex and vortex step formulations. Damiani et al. (2019) introduced the VSM to the AWE field, using the vortex core model of Bhagwat and Leishman (2002) with a fixed vortex core radius equal to 5% of the filament length (Garrel, 2003). The fundamental LL equation, e.g., shown by Anderson et al. (1980), was used for circulation–matching with nonlinear airfoil polars. Because the three-quarter-chord point was used to calculate the induced velocity, it was computed as the difference between the 3D and 2D contributions, a method based on (Piszkin and Levinsky, 1976; Ranneberg, 2015). Ferrari (2023) compared the VSM with lower-fidelity aerodynamic models for fixed-wing AWE applications and concluded that the VSM improves the representation of nonlinear spanwise loading and induced drag while remaining computationally compatible with real-time flight simulation. Cayon et al. (2023) developed a VSM
115 formulation for aero-structural coupled simulations based on Damiani et al. (2019). In this implementation, the lift magnitude is evaluated at the three-quarter-chord control point, while the lift direction is determined from the local flow angle at the
120 quarter-chord point, following the two-point interpretation proposed by Li et al. (2022).

Collectively, these contributions have transformed Prandtl’s original LL concept into a family of flexible formulations that accommodate non-planar geometries and nonlinear sectional aerodynamics, and which in modern applications is most often realised as circulation–matching LL methods coupling inviscid induction to viscous two-dimensional airfoil polars. The specific



VSM implementation presented in this paper is a modern member of this family, whose predictive capability hinges critically
125 on implementation details and the availability of representative airfoil polars for each spanwise wing section.

1.2 Problem statement and objective

For conventional airfoils, aerodynamic polars are commonly generated using tools such as XFOIL (Drela, 2013), which
couples an inviscid panel method to an integral boundary-layer formulation in a viscous–inviscid interaction framework. For
LEI kites, however, the inflated leading-edge tube induces persistent pressure-side separation and recirculation across the full
130 range of angles of attack (Folkersma, 2022), thereby violating the thin, predominantly attached boundary-layer assumptions
underlying such methods. Consequently, inviscid solvers are not suitable for predicting the 2D flow around such geometries,
requiring higher-fidelity viscous simulations, typically based on RANS equations (Folkersma et al., 2019). This, however,
considerably increases computational demand, especially in the context of iterative aero-structural coupling, where the VSM
discretises the wing into multiple deforming spanwise sections, each requiring its own polar data.

135 To substantially reduce computational effort, Breukels (2011) conducted extensive 2D RANS CFD simulations for a pa-
rameterised family of LEI airfoils and derived a correlation model for airfoil polars. In this formulation, C_L is represented by
a third-degree polynomial in the angle of attack α , whereas C_D and C_M are represented by second-degree polynomials. The
polynomial coefficients are expressed as functions of the airfoil thickness ratio t and camber parameter κ , facilitating efficient
interpolation of aerodynamic polars within the considered range of airfoil geometries. While substantially reducing computa-
140 tional cost, the approach introduces several limitations, including discontinuities arising from empirical extrapolation beyond
the simulated angle of attack range. Watchorn (2023) performed new 2D RANS CFD simulations and reported systematic
deviations with Breukels for comparable airfoils.

Having merely a fast model isn't sufficient; numerical models require rigorous validation to earn industry trust and deliver
a meaningful impact. Although 3D RANS CFD data provides a way to benchmark the performance of lower-fidelity methods
145 in incidence and sideslip (Duport et al., 2019), wind-tunnel testing is preferred. To remove structural and aeroelastic effects, a
rigidized subscale model of the TU Delft LEI V3 kite was tested with a six-component load balance and stereoscopic particle
image velocimetry to quantify forces and flow fields (Poland et al., 2025a, b). In a separate campaign on LEI airfoils, a
stethoscope, infrared cameras, zigzag tape, pressure strips, and a pitot-tube rake were used to measure loads, assess forced
transition, and characterise the flow (van Lith, 2025).

150 This study investigates the aerodynamic modelling of soft-wing kites using the V3 kite as the reference system, leveraging
the open-source available datasets and further establishing it as a community benchmark. The aerodynamic behaviour was
simulated using an extended VSM. To provide reliable predictions at low computational cost, machine-learning models were
trained using 2D RANS CFD simulations. The substitution of potential-flow-based surrogate models with an RANS-trained
machine-learning model was evaluated against flat-plate data and 2D wind-tunnel measurements (van Lith, 2025). The influ-
155 ence of the source of 2D input polars on 3D performance was assessed by comparison with wind-tunnel experiments (Poland
et al., 2025b) and 3D RANS CFD simulations (Viré et al., 2022). The study further examines VSM convergence characteris-

tics, establishes recommended best practices, and derives rigid-body stability derivatives. Finally, kite design considerations are discussed by analysing the effects of variations in airfoil shape, planform configuration, and tow-point position.

The remainder of this paper is organised as follows. Section 2 describes the VSM, Sect. 3 introduces the 2D RANS CFD setup, and Sect. 4 introduces the deployed machine learning model generation and evaluation for 2D LEI airfoils. The results are discussed in Sect. 5 and design considerations are provided in Sect. 6.

2 Vortex step method

The implemented method assumes steady flow around the lifting surface, such that the solution is restricted to the spatial domain and the starting vortex, presumed far downstream, can be neglected. For circulation–matching, the flow is decomposed into a near-field region in the vicinity of each spanwise section and a surrounding far-field region dominated by three-dimensional induction effects. The effect of the flow in the near-field region is characterised by nonlinear viscous airfoil polars that govern sectional aerodynamic lift, drag, and moment, while the far-field flow induced by the bound and trailing vortices is treated as inviscid, incompressible, and irrotational within the vortex-filament framework. These regions are coupled at a single spanwise location per section, namely the control point, where the Kutta–Joukowski theorem relates sectional circulation to the integrated lifting force. The VSM computes the aerodynamic properties of a given wing through a number of steps, illustrated in Fig. 2 and described in order in Sects. 2.1, 2.2, 2.3, 2.4, and 2.5.

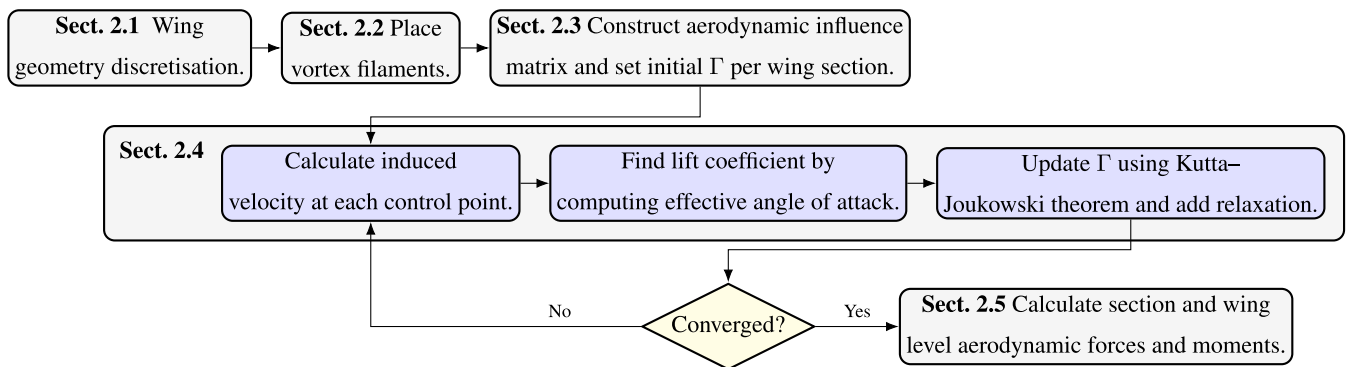


Figure 2. Flowchart of the VSM, integrating the table-of-contents structure. The three stacked layers represent preprocessing (top layer), iterative circulation matching (middle layer, Sect. 2.4), and postprocessing (bottom layer). After geometry discretisation and initialisation, the spanwise circulation distribution Γ is solved iteratively until convergence, after which the sectional and global aerodynamic coefficients are evaluated.

2.1 Wing geometry discretisation

To ensure methodological consistency, the geometry of the TU Delft V3 kite was adopted from previous CFD studies (Viré et al., 2020, 2022) and wind tunnel experiments with a rigid scale model (Poland et al., 2025a, b).

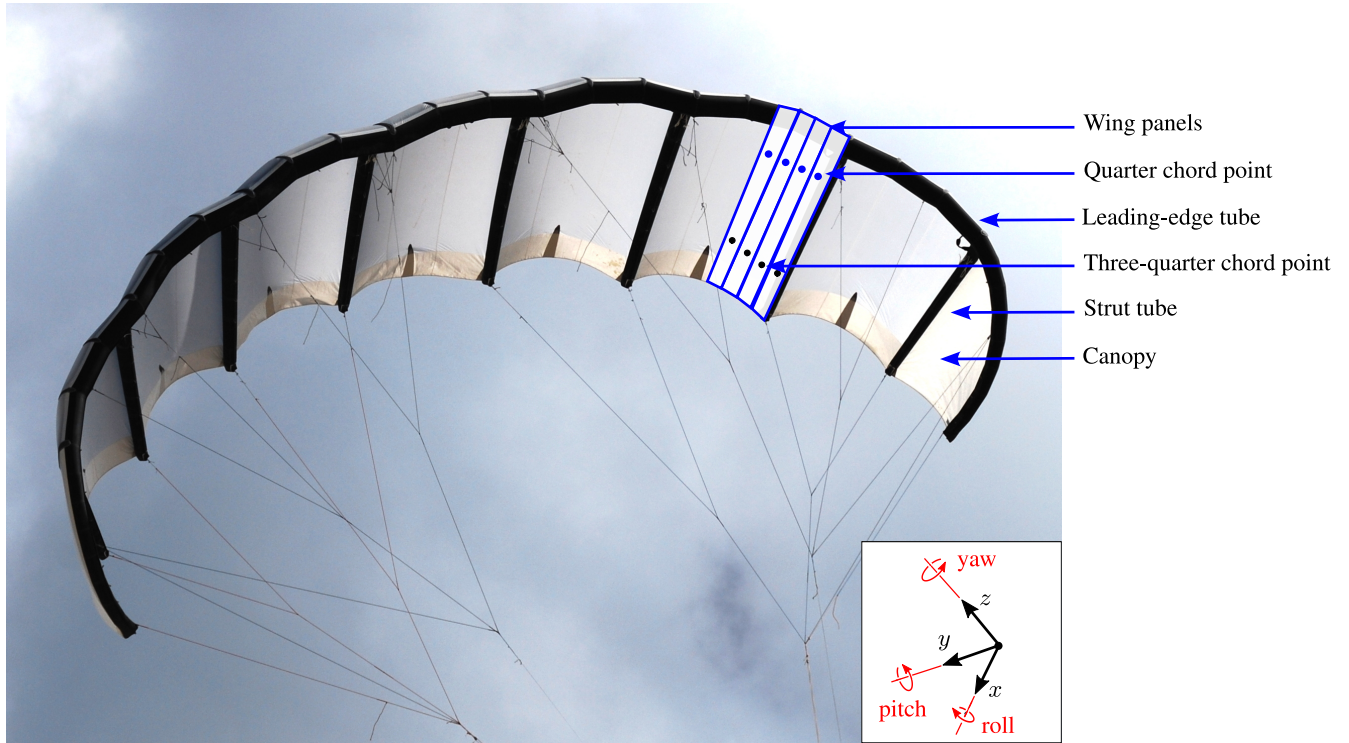


Figure 3. Photograph of the TU Delft V3 kite taken in 2012, with wing panels superimposed for illustration purposes. The quarter-chord and three-quarter-chord points for each panel are indicated. The wing reference frame is defined with the x -axis aligned with the mid-span chord-line, the y -axis oriented towards the left tip (when looking from the front) parallel to the LE tube at mid-span, and the z -axis oriented in the direction of the bridle lines.

175 Representative airfoils were extracted as chordwise slices through the wing, see Fig. A1 in App. A. The discrete spanwise locations lie on the spanwise reference line defined by connecting the quarter-chord points, obtained at each station as

$$\mathbf{x}_{c/4} = \mathbf{x}_{LE} + 0.25(\mathbf{x}_{TE} - \mathbf{x}_{LE}). \quad (1)$$

At each location, the section plane contains the global x -direction and is oriented such that its normal is perpendicular to the local surface normal at $\mathbf{x}_{c/4}$.

180 A formulation with planes aligned with the global x -axis was selected rather than one oriented locally normal to the quarter-chord line. Although both formulations are equivalent in the linear lift regime, the latter introduces additional geometric nonlinearities once $C_1(\alpha)$ departs from linear behaviour, which may bias the predicted load distribution Fritz (2024).

The wing is discretised into n_p panels, each constituting a fundamental element of the solver. The number of panels is not required to coincide with the number of chordwise slices used to define the geometry. For instance, when adopting a uniform
 185 panel distribution, both geometric properties (LE and TE coordinates) and aerodynamic properties (2D polars) defined at the chordwise slices may be interpolated to an arbitrary value of n_p .



Because the panels are rectangular, they do not form a geometrically continuous surface representation. Instead, the panel system serves to define the bound and trailing vortex filaments, rather than to reproduce the exact wing geometry.

2.2 Vortex filament system

190 Following Kelvin's circulation theorem and Helmholtz's vortex theorems, all vortex elements must form a closed system; vortices cannot spontaneously appear or vanish within the fluid (Batchelor, 1967). Accordingly, the bound vortex filament, placed at the quarter-chord line of each panel, is connected to a trailing vortex filament that extends in the chordwise direction to the TE, see Fig. 4. At the TE, these are attached to wake filaments, which extend to infinity in the free stream direction u_∞ in accordance with the frozen wake assumption (Ranneberg, 2015). At infinity, the wake filaments are closed by an
 195 additional filament, thereby completing the vortex system. This closing filament is not explicitly modelled, as its aerodynamic influence at infinite distance is assumed negligible. The resulting vortex structure is known as a horseshoe vortex. Helmholtz's theorems further require that the circulation strength remains constant along the length of each vortex filament (Batchelor, 1967); therefore, each panel has a single circulation value.

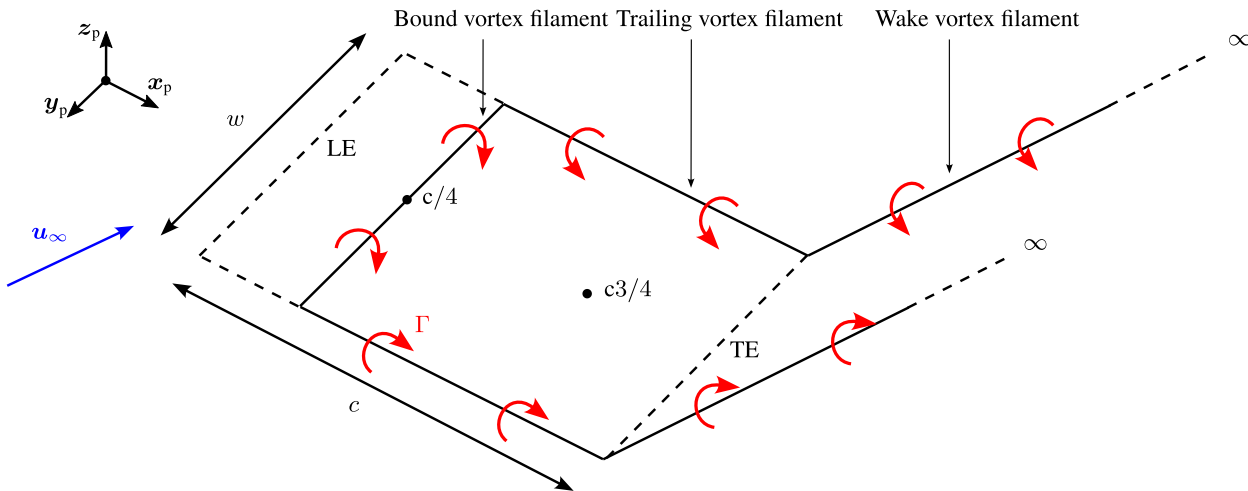


Figure 4. Illustration of a single panel, showing the incoming free-stream velocity u_∞ in blue and the circulation Γ around each filament in red. The local panel reference frame, defined by the axes x_p , y_p , and z_p , is indicated. The positions of the LE, TE, quarter-chord point $c/4$, and three-quarter-chord point $c3/4$ are also shown. Additionally, the panel chord c and panel width w are displayed.

The induced velocity vector u_{ind} at an evaluation point x due to a finite, 3D bound vortex filament or chord-aligned trailing
 200 vortex filament is computed using the Biot–Savart law (Damiani et al., 2019):

$$u_{\text{ind}} = \frac{\Gamma}{4\pi} \frac{\mathbf{r}_1 \times \mathbf{r}_2}{\|\mathbf{r}_1 \times \mathbf{r}_2\|^2} \left(\mathbf{r}_0 \cdot \left(\frac{\mathbf{r}_1}{\|\mathbf{r}_1\|} - \frac{\mathbf{r}_2}{\|\mathbf{r}_2\|} \right) \right), \quad (2)$$

where Γ is the circulation strength, \mathbf{r}_1 and \mathbf{r}_2 are vectors from the filament endpoints to x , and \mathbf{r}_0 is the vector along the filament segment.



For the wake filaments, which are modelled as semi-infinite vortex filaments, the induced velocity at \mathbf{x} is given by (Ranneberg, 2015):

$$\mathbf{u}_{\text{ind, wake}} = \frac{\Gamma}{4\pi} \left(1 + \frac{\mathbf{r}_1 \cdot \hat{\mathbf{u}}_\infty}{\|\mathbf{r}_1\|} \right) \frac{\mathbf{r}_1 \times \hat{\mathbf{u}}_\infty}{\|\mathbf{r}_1 \times \hat{\mathbf{u}}_\infty\|^2}, \quad (3)$$

where \mathbf{r}_1 is the vector from the filament origin to the evaluation point, and $\hat{\mathbf{u}}_\infty = \mathbf{u}_\infty / \|\mathbf{u}_\infty\|$ is the wake-direction unit vector.

A vortex core model was employed to avoid singular behaviour by reducing the induced velocity at points located within a specified core radius, ϵ . For bound vortex filaments, the core radius is defined as a fixed fraction of the filament length; here 5% was adopted (Garrel, 2003; Damiani et al., 2019). For trailing and semi-infinite wake filaments, a viscous core model is adopted, with the core radius given by

$$\epsilon = 2\sqrt{\frac{\alpha_0 \nu \ell}{\|\mathbf{u}_\infty\|}}, \quad (4)$$

where $\alpha_0 = 1.25643$ is the Oseen parameter, ν the kinematic viscosity, ℓ the relevant filament length.

For bound and finite trailing filaments, core regularisation is applied for $d_\perp < \epsilon$ by evaluating the Biot–Savart velocity at the radially projected point \mathbf{x}_{proj} on the core boundary and scaling linearly,

$$\mathbf{u}_{\text{ind, core}}(\mathbf{x}) = \frac{d_\perp}{\epsilon} \mathbf{u}_{\text{ind}}(\mathbf{x}_{\text{proj}}), \quad d_\perp < \epsilon. \quad (5)$$

The perpendicular distance to the filament centreline is

$$d_\perp = \frac{\|\mathbf{r}_1 \times \mathbf{r}_0\|}{\|\mathbf{r}_0\|}, \quad (6)$$

and \mathbf{x}_{proj} is constructed by keeping the axial projection of \mathbf{x} onto the filament and setting its radial distance to ϵ .

For semi-infinite wake filaments, ϵ represents a viscous core of the far wake and is used only to desingularise the Biot–Savart kernel near the centreline. The corresponding perpendicular distance is

$$d_{\perp, \infty} = \|\mathbf{r}_1 \times \hat{\mathbf{u}}_\infty\|, \quad (7)$$

and for $d_{\perp, \infty} < \epsilon$ the induced velocity is evaluated at the projected point \mathbf{x}_{proj} without additional $d_{\perp, \infty} / \epsilon$ scaling,

$$\mathbf{u}_{\text{ind, core}}(\mathbf{x}) = \mathbf{u}_{\text{ind}}(\mathbf{x}_{\text{proj}}), \quad d_{\perp, \infty} < \epsilon. \quad (8)$$

2.3 Aerodynamic influence coefficient matrix

To reduce computational cost during the circulation-matching iterations, the aerodynamic influence coefficients were precomputed once. Let $\mathbf{A} \in \mathbb{R}^{3n_p \times n_p}$ denote the block AIC matrix that maps the spanwise circulation vector $\boldsymbol{\Gamma} \in \mathbb{R}^{n_p}$ to the induced velocity at each control point. For panel $i = 1, \dots, n_p$, the induced velocity is given by

$$\mathbf{u}_{\text{ind}, i} = \sum_{j=1}^{n_p} \mathbf{A}_{ij} \Gamma_j, \quad (9)$$



230 where $\mathbf{A}_{ij} \in \mathbb{R}^{3 \times 1}$ denotes the (i, j) block of \mathbf{A} and represents the induced velocity at control point i due to a unit circulation on panel j .

To ensure compatibility with nonlinear airfoil polars, the near-field two-dimensional self-induced contribution of panel i is subtracted at its own control point to avoid double-counting induction effects already embedded in the sectional polar data (Ranneberg, 2015; Damiani et al., 2019; Cayon et al., 2023). Define the per-unit-circulation two-dimensional self-induced influence vector at control point i as

$$\mathbf{a}_{\text{ind},2\text{D},i} = \frac{1}{2\pi} \frac{\hat{\mathbf{y}}_{p,i} \times (\mathbf{x}_i - \mathbf{x}_{0,i})}{\|\mathbf{x}_i - \mathbf{x}_{0,i}\|^2}, \quad (10)$$

where $\hat{\mathbf{y}}_{p,i}$ is the local spanwise unit vector, and $\mathbf{x}_i - \mathbf{x}_{0,i}$ is the displacement from the bound-vortex centre of panel i to its control point. For a given circulation Γ_i , the corresponding two-dimensional self-induced velocity is

$$\mathbf{u}_{\text{ind},2\text{D},i} = \Gamma_i \mathbf{a}_{\text{ind},2\text{D},i}. \quad (11)$$

240 The effective induced velocity used for circulation matching is then

$$\mathbf{u}_{\text{eff},i} = \mathbf{u}_{\text{ind},i} - \mathbf{u}_{\text{ind},2\text{D},i}. \quad (12)$$

This subtraction is applied only to the self-induced contribution of panel i and not to the cross-induced contributions from other panels.

2.4 Iterative solving for circulation

245 With the AIC matrix assembled, the spanwise circulation distribution was determined iteratively. At iteration k , the induced velocity vectors at all control points were computed collectively as

$$\text{vec}(\mathbf{U}_{\text{ind}}^{(k)}) = \mathbf{A} \mathbf{\Gamma}^{(k)}, \quad (13)$$

where $\text{vec}(\cdot)$ denotes stacking of the three velocity components over all control points, and $\mathbf{U}_{\text{ind}}^{(k)} \in \mathbb{R}^{n_p \times 3}$ is the corresponding reshaped matrix whose i th row contains $\mathbf{u}_{\text{ind},i}^{(k)}$.

250 The effective relative velocity at the control point of panel i was then obtained by adding the local freestream velocity $\mathbf{u}_{\infty,i}$ to the induced velocity:

$$\mathbf{u}_{\text{rel},i}^{(k)} = \mathbf{u}_{\infty,i} + \mathbf{u}_{\text{ind},i}^{(k)}, \quad (14)$$

For each panel i , the sectional lift coefficient $C_{1,i}^{(k)}$ was obtained from the 2D polar using the effective angle of attack $\alpha_{\text{eff},i}^{(k)}$,

$$\alpha_{\text{eff},i}^{(k)} = \arctan \left(\frac{\mathbf{u}_{\text{rel},i}^{(k)} \cdot \hat{\mathbf{z}}_{p,i}}{\mathbf{u}_{\text{rel},i}^{(k)} \cdot \hat{\mathbf{x}}_{p,i}} \right), \quad (15)$$

255 where $\hat{\mathbf{x}}_{p,i}$, $\hat{\mathbf{y}}_{p,i}$, and $\hat{\mathbf{z}}_{p,i}$ denote the local chordwise (LE-to-TE), spanwise, and panel-normal (upward) unit vectors, respectively.



The circulation at each panel was updated using the Kutta–Joukowski theorem, normalised by the local reference velocity magnitude:

$$\Gamma_{\text{new},i}^{(k)} = \frac{1}{2} \frac{\|\mathbf{u}_{\text{rel},i}^{(k)} \times \hat{\mathbf{y}}_{\text{p},i}\|^2}{\|\mathbf{u}_{\infty,i} \times \hat{\mathbf{y}}_{\text{p},i}\|} c_i C_{l,i}^{(k)}, \quad (16)$$

260 where c_i denotes the local chord length.

To ensure numerical stability, under-relaxation was applied globally to the circulation array,

$$\mathbf{\Gamma}^{(k+1)} = (1 - f_{\text{relax}})\mathbf{\Gamma}^{(k)} + f_{\text{relax}}\mathbf{\Gamma}_{\text{new}}^{(k)}. \quad (17)$$

The convergence metric δ_{Γ} was defined as the normalised maximum change in the global circulation distribution between successive iterations,

$$265 \quad \delta_{\Gamma} = \frac{\max |\mathbf{\Gamma}^{(k+1)} - \mathbf{\Gamma}^{(k)}|}{\max |\mathbf{\Gamma}^{(k+1)}|}. \quad (18)$$

2.5 Converting to global properties

Once convergence was reached, the local aerodynamic force on each panel was computed as

$$\mathbf{F}_i = \frac{1}{2} \rho u_{\text{rel},i}^2 (C_{l,i} \hat{\mathbf{n}}_i + C_{d,i} \hat{\mathbf{t}}_i) c_i w_i, \quad (19)$$

270 where ρ is the fluid density, and $C_{l,i}$ and $C_{d,i}$ are the sectional lift and drag coefficients, respectively, evaluated at the three-quarter-chord control point. In other words, the local angle of attack evaluated at the three-quarter chord was used to obtain the aerodynamic coefficients from the 2D input data. The magnitude $u_{\text{rel},i}$ corresponds to the in-plane component of the relative velocity vector $\mathbf{u}_{\text{rel},i}$,

$$u_{\text{rel},i} = \|\mathbf{u}_{\text{rel},i} \times \hat{\mathbf{y}}_{\text{p},i}\|. \quad (20)$$

275 The force direction was set by an in-plane effective-flow direction following (Ranneberg, 2015; Jonkman, 2021; Damiani et al., 2019), which differed from the approach suggested by Li et al. (2022) and implemented by Cayon et al. (2023). Motivated by comparing simulations of two geometries with wind tunnel measurements, detailed in App. B.

For each panel $i = 1, \dots, n_{\text{p}}$, the in-plane drag-direction unit vector is defined as

$$\hat{\mathbf{t}}_i = \frac{\cos(\alpha_{\text{eff},i}) \hat{\mathbf{x}}_{\text{p},i} + \sin(\alpha_{\text{eff},i}) \hat{\mathbf{z}}_{\text{p},i}}{\|\cos(\alpha_{\text{eff},i}) \hat{\mathbf{x}}_{\text{p},i} + \sin(\alpha_{\text{eff},i}) \hat{\mathbf{z}}_{\text{p},i}\|}. \quad (21)$$

The lift was oriented in the normal direction $\hat{\mathbf{n}}_i$, which was constructed as

$$280 \quad \hat{\mathbf{n}}_i = \frac{\hat{\mathbf{t}}_i \times \hat{\mathbf{y}}_{\text{p},i}}{\|\hat{\mathbf{t}}_i \times \hat{\mathbf{y}}_{\text{p},i}\|}. \quad (22)$$

The local aerodynamic moment on a panel i was defined as

$$\mathbf{M}_i = \frac{1}{2} \rho u_{\text{rel},i}^2 C_{m,i} \hat{\mathbf{y}}_{\text{p},i} w_i c_i^2, \quad (23)$$



where $C_{m,i}$ is the sectional moment coefficient and w_i is the panel width; this moment represents the pitching moment about the quarter-chord point of the panel, consistent with the definition of $C_{m,i}$.

285 The contributions of all panels were summed and projected onto both the global coordinate directions \hat{e}_x , \hat{e}_y , and \hat{e}_z , and the body-fixed aerodynamic directions: drag \hat{e}_D , aligned with \mathbf{u}_∞ ; lift \hat{e}_L , perpendicular to drag; and side \hat{e}_S , orthogonal to both drag and lift. With $U_\infty = \|\mathbf{u}_\infty\|$, the resulting non-dimensional force and moment coefficients are

$$C_j = \frac{2}{\rho U_\infty^2 S} \sum_{i=1}^{n_p} \mathbf{F}_i \cdot \hat{e}_j, \quad \text{for } \hat{e}_j \in \{\hat{e}_x, \hat{e}_y, \hat{e}_z, \hat{e}_D, \hat{e}_L, \hat{e}_S\}, \quad (24)$$

$$C_{M,j} = \frac{2}{\rho U_\infty^2 S c_{\text{ref}}} \sum_{i=1}^{n_p} [\mathbf{M}_i + (\mathbf{r}_{c/4,i} - \mathbf{r}_0) \times \mathbf{F}_i] \cdot \hat{e}_j, \quad \text{for } \hat{e}_j \in \{\hat{e}_x, \hat{e}_y, \hat{e}_z\}. \quad (25)$$

290 where S is the projected planform area, c_{ref} the reference chord length, n_p the number of panels, $\mathbf{r}_{c/4,i}$ the quarter-chord location about which the moment is defined for each panel, \mathbf{r}_0 the chosen global reference point, and \hat{e}_j the projection direction.

The centre of pressure \mathbf{r}_{cp} was determined by

$$\mathbf{r}_{\text{cp}} = \mathbf{r}_0 + \frac{\mathbf{F} \times \mathbf{M}_0}{\|\mathbf{F}\|^2}, \quad (26)$$

where \mathbf{F} is the combined aerodynamic force vector of the wing, and \mathbf{M}_0 is the combined moment vector about the reference point \mathbf{r}_0 , and $\|\mathbf{F}\|$ denotes the Euclidean norm of \mathbf{F} . The resulting vector \mathbf{r}_{cp} lies along the line of action of the aerodynamic force and represents the unique point where this line intersects the wing surface. This intersection defines the effective location at which the resultant force can be considered to act, and it provides a critical indicator of aerodynamic stability, especially in relation to the trim state of the kite.

3 Airfoil aerodynamics

300 This section outlines the modelling framework used to generate aerodynamic airfoil data. It describes the profile parameterisation, mesh generation, and simulation setup employed for the CFD analyses, followed by the convergence monitoring procedure.

3.1 Profile geometry parameterisation

The parameterisation presented herein extends the earlier approach by Breukels (2011), who introduced two fundamental parameters: the circular LE tube diameter t and the camber height κ , shown in Fig. 5. Subsequently, informed by the experimental findings of Den Boer (1980), who observed a forward shift of the maximum camber position with increasing angle of attack, the chordwise location of maximum camber η was incorporated as an essential design parameter (Watchorn, 2023). Another step was to set the trailing-edge height from $t/2$ to zero, in accordance with the conventional airfoil definition (Kappel, 2012). A TE reflex angle δ is introduced, as this is often used to enhance the static pitching moment C_m and reduce the risk of front stall.

310



The LEI kite profile is constructed by defining a circular LE tube, smoothly extending it toward the maximum camber location using a Bézier curve named the front spline, and subsequently connecting it to the TE via another Bézier curve called the rear spline, see Fig. 5. Tangent continuity is enforced at both the junction between the curves and at the TE, ensuring aerodynamic smoothness. In this way, the profile shape can be characterised through six design parameters, summarised in Table 1.

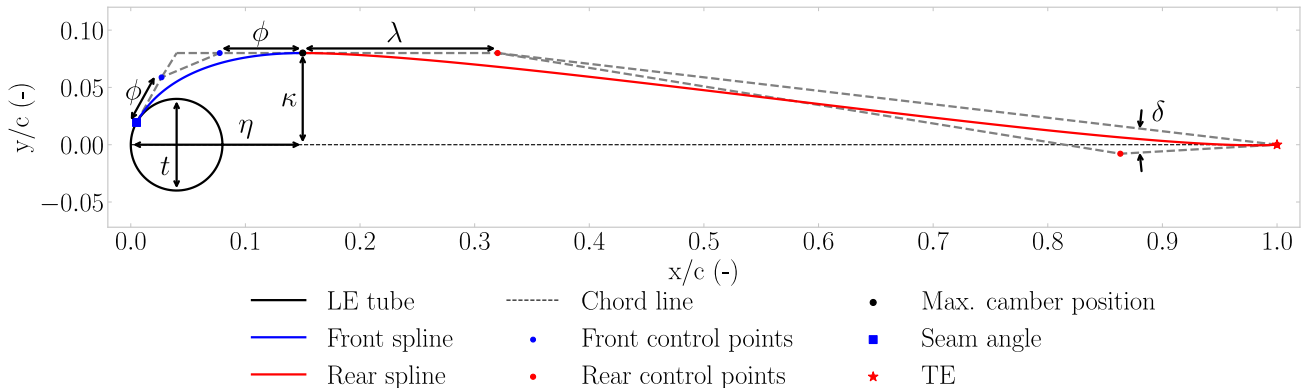


Figure 5. Overlay of the LEI kite profile parameterisations using Bézier curves.

Table 1. Overview of the profile shape parameters used in the Bézier-curve based parametrisation.

| Symbol | Unit | Description |
|-----------|------|---|
| t | – | Diameter of the inflatable leading edge tube, non-dimensionalised by chord. |
| η | – | Chordwise position of the maximum camber point, non-dimensionalised by chord. |
| κ | – | Maximum camber height, non-dimensionalised by chord. |
| δ | ° | Reflex angle, defined as the angle between the vectors from the second rear control point to the TE and the third rear control point to the TE. |
| λ | – | Camber tension was defined as the degree of curvature tightening or slackening between LE and TE, non-dimensionalised as the percentage of chordwise distance locating the first control point on the rear spline. |
| ϕ | – | LE curvature defines the placement of the control points along the tangent lines emanating from the seam angle and the maximum camber location, non-dimensionalised by the total length of the respective section, i.e., expressed as a fraction of the length of its tangent line. |

315

Each Bézier curve is defined by four control points $[P_0, P_1, P_2, P_3]$, with the parametric coordinate $t_b \in [0, 1]$ controlling the interpolation:

$$\begin{bmatrix} x \\ y \end{bmatrix} = (1 - t_b)^3 P_0 + 3(1 - t_b)^2 t_b P_1 + 3(1 - t_b) t_b^2 P_2 + t_b^3 P_3. \quad (27)$$



The front spline connects the seam angle to the maximum camber location. The seam angle, defined as the point at which the
320 LE tube is attached to the canopy, is determined using a dynamic search algorithm to ensure a smooth and tangent transition
between the LE tube and the canopy. The dynamic search algorithm increases the seam angle stepwise, until the apex points of
the resulting front spline align with the defined max camber location κ . The tangent line at the seam angle defines the directions
along which the intermediate control points are positioned, with the LE curvature parameter ϕ specifying their relative distance
along these tangents. In this way, ϕ shapes the curvature distribution: larger values concentrate curvature near the centre of the
325 curve, while smaller values shift it towards the endpoints.

The rear spline connects the maximum camber location to the TE. The intermediate control points are governed by the
camber tension parameter λ , which adjusts profile smoothness, and by the TE reflex angle δ . To enhance model robustness and
limit free parameters, the third control point is placed at 20% of the distance between the second rear control point and the TE.

3.2 Meshing

330 To ensure a smooth computational mesh, the LEI kite profile geometry requires specific adaptations. In particular, the sharp
corner at the junction between the lower canopy and the LE tube is smoothed using a fillet. In addition, a canopy thickness
 t_{canopy} is introduced to provide a realistic representation of a finite thickness, distinguish top from bottom airflow, and enable
a rounded TE. The optimal fillet size and t_{canopy} were determined through a sensitivity study; for details, the reader is referred
to Masure (2025).

335 A structured O-grid mesh, shown in Fig. 6, was generated for each profile using a hyperbolic-Laplace solver in POINT-
WISE (Pointwise, 2025), automated via a Python script. An O-grid topology was selected primarily for its insensitivity to
variations in angle of attack, which reduces computational cost as only one mesh has to be generated per profile. Each pro-
file was embedded in a computational domain extruded by one chord length in the z -direction. The far-field boundary was
modelled as a cylindrical region extending 201 cell layers outward from the profile, with a unit depth of length 1.

340 For all cases, smoothing parameters for hyperbolic extrusion in POINTWISE were applied uniformly to ensure mesh quality
and numerical stability. The explicit smoothing parameter was set to eight for transverse smoothing, while the implicit param-
eter was set to 16.0. Kinsey-Barth smoothing, with a value of five, was used in the wall-normal direction to address regions of
strong concavity. The volume smoothing parameter was set to its default value of 0.5.

Node spacing was uniform near the LE and TE, while a hyperbolic tangent distribution was applied along the canopy surface
345 to minimise abrupt grid transitions. Mesh independence was confirmed by refining the grid until the lift and drag coefficients
no longer showed variation with further grid refinement (Masure, 2025).

Wall-normal mesh layers are generated by hyperbolic extrusion, with a fixed growth rate of 1.1 following Watchorn (2023).
To accurately resolve the boundary layer, the mesh included prismatic inflation layers with a wall-normal first cell height
chosen to ensure $y_{\text{max}}^+ < 1$ over the entire airfoil. The non-dimensional wall distance y^+ is defined as

$$350 \quad y^+ = \frac{\rho_{\infty} y u_{\tau}}{\mu_{\infty}}, \quad (28)$$

where ρ_{∞} denotes freestream density, μ_{∞} the dynamic viscosity, and u_{τ} the friction velocity.

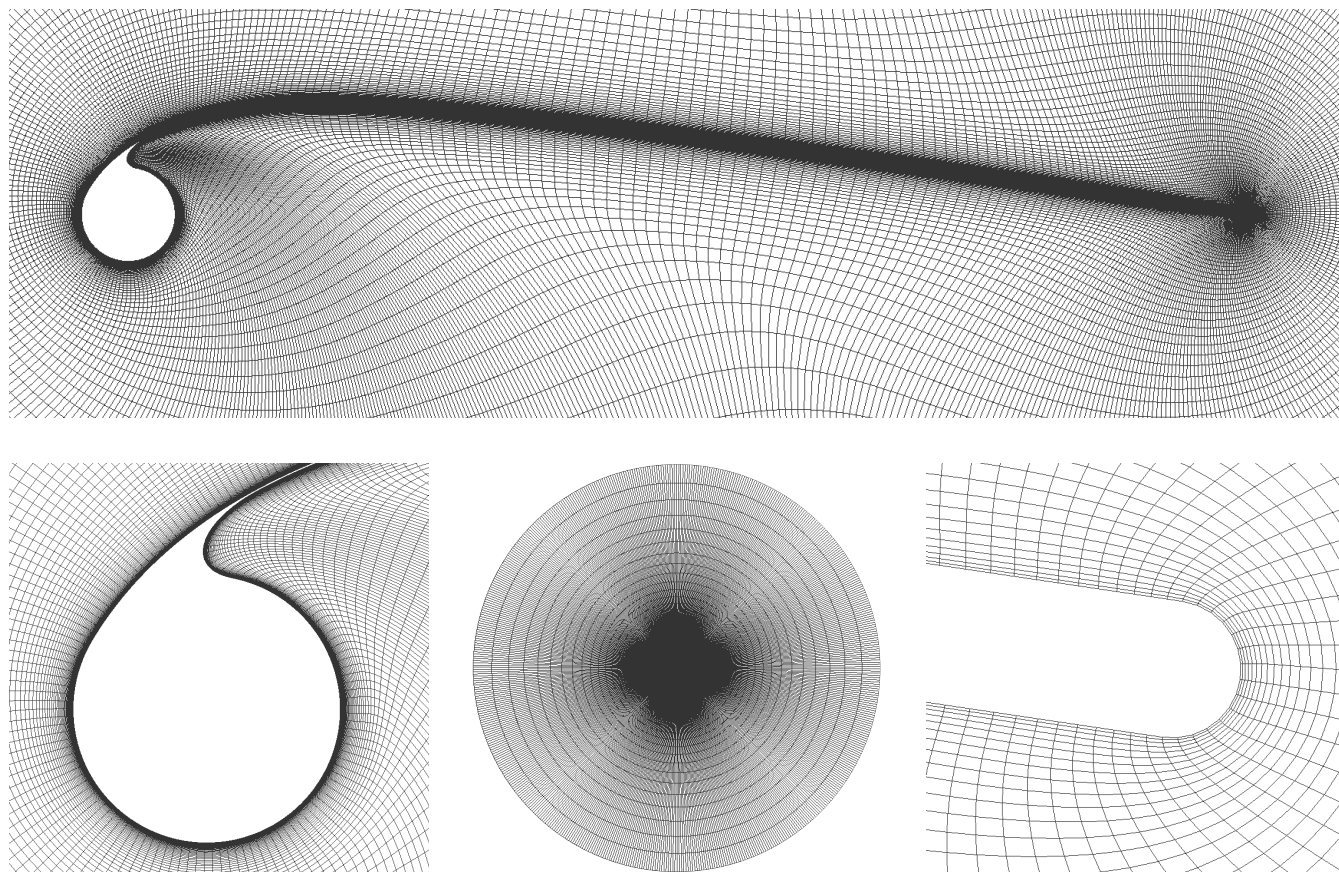


Figure 6. Fully structured mesh (575×201) for a LEI kite profile with shape parameters $t = 0.08$, $\eta = 0.15$, $\kappa = 0.08$, $\delta = 0^\circ$, $\lambda = 0.2$, and $\phi = 0.65$. The top panel shows the airfoil, and the lower panels depict, from left to right, the LE tube, the O-grid, and the TE.

3.3 Simulation Setup

By assuming steady-state and incompressible flow, the steady RANS equations were solved using OPENFOAMV2006, with pressure–velocity coupling managed internally by the semi-implicit method for pressure-linked equations (SIMPLE) algorithm (OpenFOAM, 2025). For an overview of the numerical schemes, the reader is referred to (Masure, 2025). The revised $k-\omega$ shear stress transport (SST) model by Menter (1994) was employed due to its robustness in capturing both near-wall and outer-region flow physics, supported by prior implementations in aerodynamic studies of LEI kites (Folkersma et al., 2019; Viré et al., 2020, 2022; Watchorn, 2023). All simulations were performed under the assumption of fully turbulent flow, owing to the measured turbulence intensities, the surface roughness present on both suction and pressure sides, and the high Reynolds numbers; a more elaborate discussion of this modelling choice is provided in App. C

The inlet velocity scalar u_∞ , set to 1 ms^{-1} , was projected in the direction of the angle of attack α to define the vector inlet velocity,

$$\mathbf{u}_i = u_\infty \begin{bmatrix} \cos \alpha \\ \sin \alpha \\ 0 \end{bmatrix}. \quad (29)$$

The turbulent kinetic energy k_i is defined as

$$365 \quad k_i = \frac{3}{2}(u_\infty I)^2, \quad (30)$$

where I represents the freestream turbulence intensity. The specific dissipation rate ω_i at the inlet was defined as

$$\omega_i = \frac{k_i}{\nu_\infty} \left(\frac{\nu_t}{\nu_\infty} \right)^{-1}, \quad (31)$$

where ν_t/ν_∞ represents the eddy viscosity ratio. Values of $I = 2\%$ and $\nu_t/\nu_\infty = 10$ were selected based on the sensitivity studies of Folkersma et al. (2019); Viré et al. (2020).

370 Boundary conditions for velocity \mathbf{u} , kinematic pressure p_k , turbulent kinetic energy k , specific dissipation rate ω , and eddy viscosity ν_t were applied as summarised in Table 2. Far-field boundaries employed non-reflecting types; the airfoil surface was defined as a stationary, impermeable no-slip wall with appropriate wall functions for turbulence; and spanwise boundaries were set to EMPTY.

Table 2. Boundary conditions and units for velocity, pressure, and turbulence variables.

| Variable | Unit | Far field | Airfoil surface |
|--------------|---------------------------|-------------|-------------------|
| \mathbf{u} | ms^{-1} | INLETOUTLET | FIXEDVALUE |
| p_k | m^2s^{-2} | OUTLETINLET | ZEROGRADIENT |
| k | m^2s^{-2} | INLETOUTLET | FIXEDVALUE |
| ω | s^{-1} | INLETOUTLET | OMEGAWALLFUNCTION |
| ν_t | m^2s^{-1} | CALCULATED | NUTKWALLFUNCTION |

3.4 Convergence monitoring

375 Convergence was monitored through both equation residuals and aerodynamic force coefficients. Specifically, residuals associated with momentum, pressure, and turbulence variables u_x , u_y , p , k , and ω were required to fall below 10^{-6} (Ferziger et al., 2020), while the force coefficients C_l , C_d , and C_m were expected to converge to within 10^{-4} .

In OPENFOAM, the initial residual is used for monitoring convergence, rather than the final value. As a result, simulations exhibiting rapid convergence may not always reach the 10^{-4} force threshold. To ensure consistency across all cases, an initial
 380 residual threshold of 8×10^{-7} was applied for all flow variables. Each simulation was limited to a maximum of 5,000 iterations.



Cases not reaching the required thresholds within this limit were classified as non-converged, typically occurring at high or negative angles of attack, where steady RANS solutions become unreliable due to increased unsteadiness, e.g., flow separation.

For improved numerical stability, the velocity relaxation factor was set to 0.8, which dampened residual oscillations and improved convergence consistency. Representative histories for a typical LEI profile at $\alpha = 6^\circ$ are shown in Fig. 7, where final

385 flow residuals fell below 10^{-6} and force residuals just below 10^{-4} .

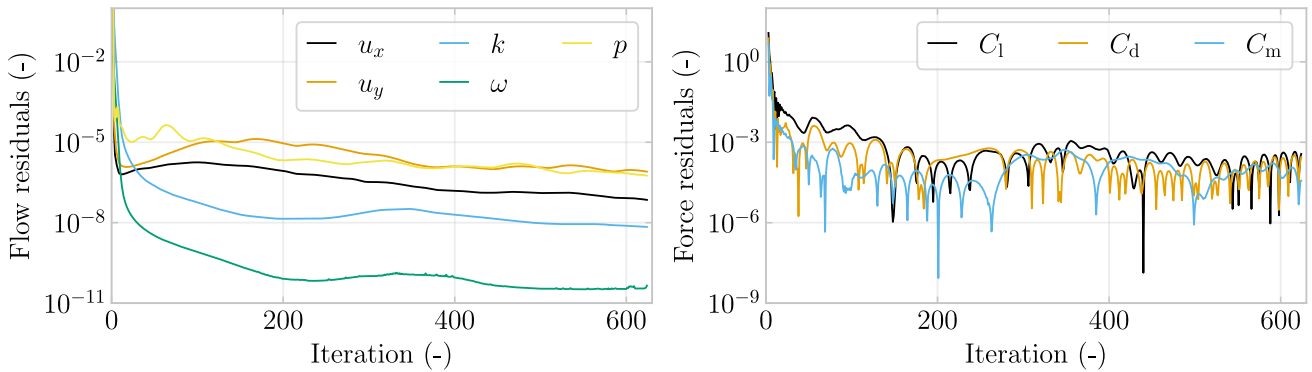


Figure 7. Flow residuals at $\alpha = 6^\circ$ for a profile with $t = 0.0782$, $\eta = 0.178$, $\kappa = 0.0953$, $\delta = 0.351$, $\lambda = 0$, $\phi = 0.1$.

4 Machine learning

This section presents the development and validation of a machine learning (ML) surrogate model trained on the aerodynamic database generated in Sect. 3. It describes the generation and filtering of the input data, the training and tuning of multiple regression algorithms, and the evaluation of their predictive accuracy for lift, drag, and moment coefficients.

390 4.1 Defining input profiles

Training data for the ML model were generated by varying the profile parameters, as shown in Table 3, over a range that encompasses physically viable profile designs. As varying ϕ within the marginal physically consistent range was found to have minimal aerodynamic influence, it was fixed at $\phi = 0.65$, allowing greater resolution of the remaining parameters. The angle of attack range and sampling density were chosen to optimise accuracy in the lift polar and maintain computational efficiency,

395 with fewer points in the linear region ($2^\circ \leq \alpha \leq 10^\circ$) and negative α , and a finer step of 2° near stall. The six-dimensional input parameter space was analyzed separately for three Reynolds numbers: $Re = 1 \times 10^6$, representative of small kites or static flight; $Re = 5 \times 10^6$, corresponding to typical in-flight operation; and $Re = 2 \times 10^7$, characteristic of larger kites and/or higher inflow velocities (Cayon et al., 2025b; Masure, 2025).



Table 3. Design parameter ranges of the generated data for $Re = 1 \times 10^6$, 5×10^6 and 2×10^7 .

| Parameter | Unit | Variables | Count |
|-----------|------|--|-------|
| t | — | 0.03, 0.06, 0.08, 0.1, 0.12 | 5 |
| η | — | 0.08, 0.1, 0.15, 0.2, 0.25, 0.3, 0.35, 0.4 | 8 |
| κ | — | 0.04, 0.06, 0.08, 0.1, 0.12, 0.14, 0.16 | 7 |
| δ | ° | -8, -5, -2, 0 | 4 |
| λ | — | 0.1, 0.2, 0.3, 0.4 | 4 |
| α | ° | -10, -5, -2, 0, 2, 6, 10, 12, 14, 16, 18, 20, 22 | 13 |

In pre-processing, the profiles were filtered out if the camber tension control point λ was positioned too far aft, i.e. $\eta + \lambda \geq 0.8$, or if the camber height κ was excessively large, i.e. $\kappa > 2.5t$. After filtering, 3,464 configurations remained per angle of attack, resulting in 45,032 simulations per Reynolds number.

4.2 Input data generation

For each profile parameter combination, a mesh was generated locally and used for RANS CFD simulations across the required angles of attack and Reynolds numbers on the HPC-12 cluster at Delft University of Technology, requiring a total of 1.4×10^5 core hours. A limited number of cases did not converge within 5,000 iterations, predominantly at high angles of attack beyond stall, and were subsequently removed from the data.

Additionally, a z -score filtering approach (Dekking et al., 2005),

$$z = \frac{x - \mu}{\sigma}, \quad (32)$$

where μ represents the mean and σ the standard deviation, was used to identify and remove statistical outliers. Specifically, for each α and force coefficients, any data point with an absolute z -score greater than three standard deviations from the mean was classified as an outlier and removed, illustrated in Fig. 8.

Profiles with a max camber smaller than radius, i.e. $\kappa < \frac{t}{2}$, are defined as camber-limited profiles and represent 0.23% of the training data set. For these cases, the number of parameters affecting the front and rear splines was reduced to t and δ , since the removed parameters had little to no effect. The camber-limited profiles exhibit distinct aerodynamic characteristics, producing lower lift and stalling earlier at approximately $\alpha = 10^\circ$. Consequently, they exhibit relatively high drag coefficients post-stall and increased pitching moments, indicating a stronger nose-up tendency in pre-stall flight conditions.

Building a predictive model within this design space requires the definition of both training and test datasets. A separate test data set was constructed at different angles of attack from those used in the training set, to verify the predictions at an α at which the model was not trained, shown in Table 4. After removing non-converged cases and statistical outliers, as summarised in Table 4, the final dataset comprises 42,183 training samples and 5,016 test samples, corresponding to a test-train split of

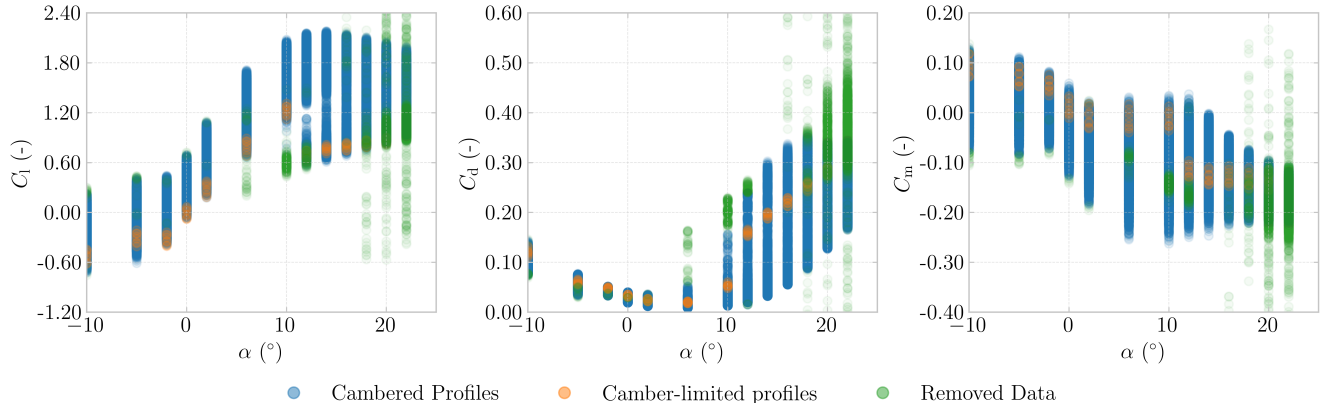


Figure 8. Aerodynamic coefficients versus angle of attack for the $Re = 5 \times 10^6$ dataset, illustrating filtering of cambered profiles, camber-limited profiles, and removed data.

10.6%. The test data set exhibited a higher overall convergence rate, which was attributed to its narrower angle-of-attack bounds, making convergence less prone to failure near the limits, i.e., at negative α or under stall conditions.

Table 4. Data filtering steps and resulting sizes for $Re = 5 \times 10^6$ dataset.

| Step | Train data | Test data | Test data α ($^\circ$) |
|-------------------------|---------------|-------------|---------------------------------|
| Simulated data | 45,032 | 5,187 | -8, -3.3, -1, 1.2, |
| Not converged (removed) | 2,452 (5.45%) | 118 (2.27%) | 2.5, 4, 5.3, 8, 11, |
| Outliers (removed) | 397 (0.93%) | 53 (1.05%) | 14.4, 17, 18.5, 21 |
| Final dataset size | 42,183 | 5,016 | - |

4.3 Model set-up

A separate ML model was trained for each Re to predict C_l , C_d , and C_m from any given set of the design parameters, resulting in a model with a six-dimensional input space and a three-dimensional output space. The three quantities were selected because they represent key aerodynamic metrics and allow for the determination of the chordwise centre of pressure, x_{cp} , which is a crucial stability indicator. Using lift, drag, and moment, one obtains

$$x_{cp} = x_{ref} - \frac{C_m c}{\sqrt{C_l^2 + C_d^2} \sin\left(\tan^{-1}\left(\frac{C_l}{C_d}\right) + \alpha\right)}, \quad (33)$$

which yielded values within 1% of those obtained by pressure integration (Masure, 2025).

Model development began with standardising the filtered training datasets, after which several regression algorithms were evaluated using their default settings (Pedregosa et al., 2011). The selected models were chosen for their strong baseline



performance reported by (Pandala, 2021), and linear regression was included for reference. The full ML workflow is described in App. D and illustrated in Fig. D1.

After an initial model run with default settings, hyperparameters were systematically fine-tuned using grid search cross-validation. In this context, validation refers to the internal process of developing the regression model across different hyperparameter combinations using subsets of the training data before evaluating the final model's performance on an independent test dataset. The coefficient of determination R^2 (Dekking et al., 2005), defined as

$$R^2 = 1 - \frac{\sum_{i=1}^n (y_i - \hat{y}_i)^2}{\sum_{i=1}^n (y_i - \bar{y})^2}, \quad (34)$$

was selected as the scoring metric, where y_i denotes the true value for each data point, \hat{y}_i the corresponding model prediction, \bar{y} the mean value of the observed data, and n the number of points in the dataset. The hyperparameter search utilised a k -fold cross-validation approach, dividing the training set into $k = 10$ subsets or folds, with 90% of the data used for training and 10% for validation in each iteration. This was feasible because the dataset was sufficiently large to provide ample training data for improving model accuracy, measured here by R^2 , while still reserving a large enough test set to ensure reliability, as quantified by a low standard deviation.

To achieve smooth and accurate predictions between sampled angles of attack, a piecewise cubic Hermite interpolating polynomial (PCHIP) spline was applied to the ML model outputs, as most models lack continuity in angle of attack.

4.4 Model Selection

After tuning is finalised, the performance of each model was assessed using the test dataset by three metrics: R^2 , the percentage root mean square error,

$$\text{RMSE}_{\%} = \frac{\sqrt{\frac{1}{n} \sum_{i=1}^n (y_i - \hat{y}_i)^2}}{\langle |y_{\text{test}}| \rangle} \times 100, \quad (35)$$

and the percentage standard deviation,

$$\sigma_{\%} = \frac{\sqrt{\frac{1}{n-1} \sum_{i=1}^n (r_i - \bar{r})^2}}{\langle |y_{\text{test}}| \rangle} \times 100, \quad (36)$$

where n is the number of test samples, y_i and \hat{y}_i are the true and predicted values, $\langle |y_{\text{test}}| \rangle$ is the mean absolute value of the test targets, and r_i and \bar{r} are the residuals and their mean, respectively.

Table 5 shows the averaged results per model, from which extremely randomised trees (ERT) were selected as they outperform the other algorithms, achieving the highest R^2 and lowest $\text{RMSE}_{\%}$ and $\sigma_{\%}$.

4.5 Model evaluation

As shown in Table 6, the ERT exhibited high predictive accuracy with $R^2 > 0.98$ across all Re. The standard deviation $\sigma_{\%}$ decreased with increasing Re, indicating greater prediction consistency and improved alignment with CFD predictions at higher Re.



Table 5. ML model verification using R^2 , RMSE%, and $\sigma\%$ for the $Re = 5 \times 10^6$ model.

| ML model | Acronym | R^2 (-) | RMSE (-) | $\sigma\%$ (-) | Training time (s) |
|----------------------------|---------|-----------|----------|----------------|-------------------|
| K-nearest neighbours | KNN | 0.9576 | 18.54% | 18.28% | 0.05 |
| Linear regression | LR | 0.6169 | 55.50% | 55.08% | 0.04 |
| Random forest | RF | 0.9442 | 21.15% | 24.08% | 10.6 |
| Extremely randomized trees | ERT | 0.9857 | 10.87% | 9.83% | 9.1 |
| Support vector regression | SVR | 0.7470 | 43.10% | 18.23% | 46.3 |
| Multi-layer perceptron | MLP | 0.9366 | 22.42% | 17.02% | 7.4 |

Table 6. Regression model performance metrics per Re.

| Re (-) | $\sigma\%$ (-) | R^2 (-) | | | |
|-----------------|----------------|-----------|-------|-------|------------------|
| | | C_d | C_l | C_m | $\overline{R^2}$ |
| 1×10^6 | 10.52% | 0.989 | 0.988 | 0.985 | 0.987 |
| 5×10^6 | 9.43% | 0.984 | 0.993 | 0.987 | 0.988 |
| 2×10^7 | 7.68% | 0.983 | 0.995 | 0.990 | 0.989 |

To further evaluate the model’s performance, three distinct and representative profiles were selected from the test dataset, detailed in Table 7. The third profile is notable as it represents a camber-limited configuration. The prediction metrics for these profiles are summarised in Table 7 and illustrated in Fig. 9 for C_l , C_d and C_m . In the plots, the PCHIP spline forms a smooth connection between the ML predictions at the angle of attack values present in the training data, allowing aerodynamic
 465 coefficients to be extrapolated for comparison with the true test data.

Overall, profile 2, with $t = 0.086$ close to the LE tube thickness of the mid-span profile of the V3 kite, exhibited the highest R^2 values and the lowest RMSE% values, indicating the greatest predictive certainty. No consistent trend was observed in a specific force coefficient; for example, R^2 and RMSE% were highest either for C_d or for C_m . In general, a lower R^2 corresponded to a higher RMSE, with the RMSE% showing larger absolute changes when mispredictions occurred. For instance,
 470 in the drag polar of profile 2, two clear mispredictions increased the RMSE% by a factor of two compared with C_l , where only a single misprediction was present. The drag polars of profiles 1 and 3 revealed a similar pattern: in profile 1, one large misprediction resulted in an RMSE% approximately four times greater.

5 Results

This section reports the principal findings of the study, beginning with flow-field observations and subsequently presenting a
 475 quantitative comparison of LEI airfoil polars. In addition, the VSM was examined with respect to convergence characteristics, sensitivity to airfoil-level inputs, rigid-body stability derivatives, and a concise synthesis of best practices and limitations.



Table 7. Prediction performance metrics for Profiles 1–3.

| Profile | Profile parameters | | | | | | R^2 (-) | | | RMSE% (°) | | |
|---------|--------------------|--------|----------|----------|--------|-----------|-----------|-------|-------|-----------|-------|-------|
| | t | η | κ | δ | ϕ | λ | C_l | C_d | C_m | C_l | C_d | C_m |
| 1 | 0.032 | 0.308 | 0.047 | -3.5 | 0.65 | 0.134 | 0.980 | 0.959 | 0.931 | 11.4% | 25.3% | 25.8% |
| 2 | 0.086 | 0.192 | 0.080 | -5.6 | 0.65 | 0.325 | 0.998 | 0.996 | 0.999 | 3.3% | 6.7% | 2.3% |
| 3 | 0.115 | 0.000 | 0.000 | -7.7 | 0.00 | 0.000 | 0.950 | 0.996 | 0.955 | 19.6% | 6.0% | 31.0% |

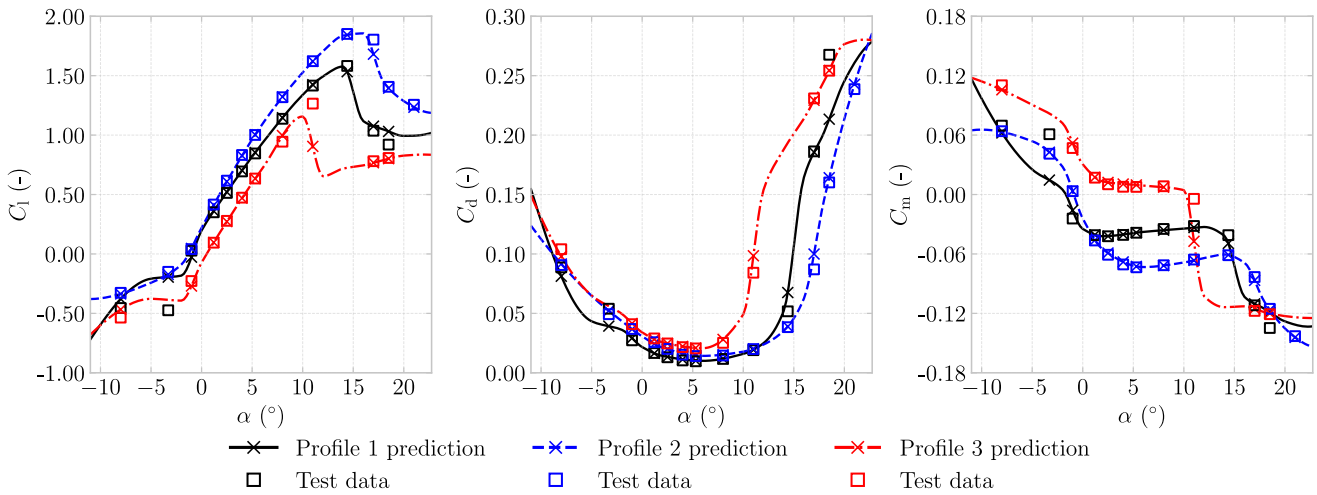


Figure 9. Verification of the ML model using lift, drag, and moment polar for the $Re = 5 \times 10^6$ dataset.

5.1 Flow field observations

The flow topology at $\alpha = 2^\circ$ and $\alpha = 8^\circ$ is shown in Fig. 10, indicating the pressure-colored streamlines around the V3 kite mid-span airfoil and the corresponding surface distributions of C_p and C_f . From the pressure-side streamlines, it is evident that a recirculation zone is present, splitting into two circulation areas. A corner-eddy closer to the tube, and a larger zone, that is more affected by inflow angle variations as it decreases in size with increasing α . The circulation direction can be inferred from the friction coefficients; a negative friction coefficient indicates a counterclockwise rotation.

At $\alpha = 8^\circ$, the C_p indicates a comparatively larger negative pressure peak at the suction side and shows a distinct upward pressure peak at the centre of the recirculation zone. Where the recirculation zone stretches to the airfoil's surface, the friction coefficient C_f displays a peak in the opposite -downward- direction. Increasing α from 2° to 8° , leads to more concentrated and negative peak. Furthermore, double values are plotted for both C_p and C_f in the region where, along a vertical line, one encounters both three pressure-side surfaces, a distinct feature of an LEI airfoil.

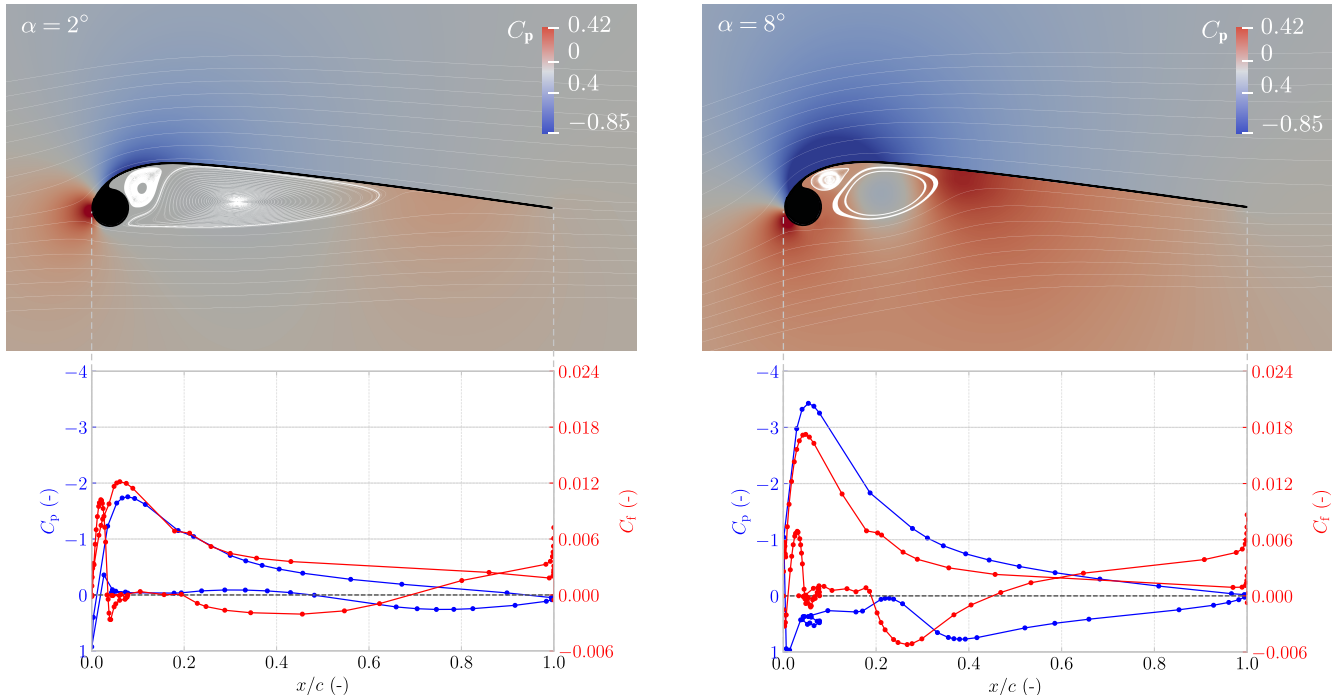


Figure 10. Flow fields at $\alpha = 2^\circ$ and $\alpha = 8^\circ$ for the V3 kite at $Re = 1 \times 10^6$. The figures present the surface pressure coefficient C_p and skin-friction coefficient C_f as functions of the non-dimensional chordwise coordinate x/c .

5.2 Simulating airfoil aerodynamics

To assess the feasibility of inviscid methods for generating aerodynamic polars, NEURALFOIL, a physics-informed surrogate model trained on tens of millions of XFOIL simulations and analytical solutions, was utilized (Drela, 2013; Sharpe, 2023, 2024). Although XFOIL, on which NEURALFOIL was trained, is not a purely inviscid method but a viscous–inviscid interaction solver, its integral boundary-layer formulation assumes a thin shear layer coupled to an outer potential flow. Once separation becomes extensive and the flow no longer resembles a thin boundary layer attached to the surface, the mathematical foundation of the model is violated, and the predicted lift, drag, and pressure distributions can no longer be considered physically reliable (Drela, 2013). Since LEI airfoils exhibit persistent pressure-side separation and recirculation that contravene these assumptions, the inclusion of NEURALFOIL permits a structured assessment of the limitations of such viscous–inviscid approaches when applied to geometries dominated by extensive separated flow.

In this study, the largest model size, `xxxlarge`, was used; it achieves maximum errors of less than 0.3% in the lift, drag, and moment coefficients relative to XFOIL (Sharpe, 2024). The boundary-layer transition was set to $x/c = 0$ to mimic the fully turbulent assumption used in the deployed 2D RANS CFD simulations.

To put the LEI airfoil aerodynamic trends in perspective, the lift and drag wind tunnel measurements of a flat plate were used (Wick, 1954). Because moment measurements were not available, the moment polar was computed following classical



flat-plate airfoil theory,

$$C_m = -\frac{\pi}{4} \sin 2\alpha, \quad (37)$$

505 where α is in radians.

The predictions from classical flat-plate theory, flat-plate wind tunnel measurements, Breukels' regression model, NEURAL-FOIL, 2D RANS CFD results, and wind tunnel measurements (van Lith, 2025), for the lift, drag, and moment coefficients are plotted as a function of α , shown in Fig. 11 for the mid-span airfoil of the V3 kite, displayed in App. A.

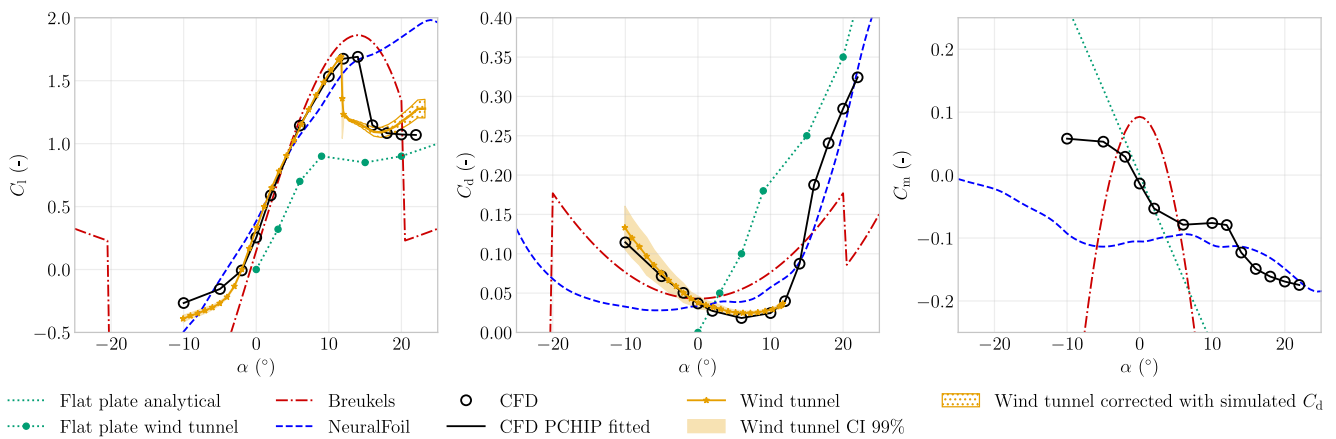


Figure 11. The figure shows the airfoil C_l , C_d , and C_m as functions of α , obtained from different sources evaluated at $Re = 10^6$. The numerical models, except for the flat plate model, assume fully turbulent flow. This was mimicked in the wind tunnel measurements using zigzag strips, applied on the suction side at 3% and on the pressure side at 45° of the tube, which were confirmed to be of sufficient height to induce transition (van Lith, 2025).

The predictions generated by Breukels' regression model were considered invalid outside the range $|\alpha| \leq 20^\circ$. At these
 510 higher angles of attack, the extrapolated polars exhibited unphysical behaviour, including lift and drag discontinuities near $\alpha = \pm 20^\circ$ and negative drag coefficients for $\alpha < -20^\circ$, which were attributed to insufficient smoothing between the empirical expressions used to extrapolate the model beyond the CFD-simulated range. Furthermore, assuming symmetry and antisymmetry about $\alpha = 0^\circ$ was considered inappropriate due to the airfoil's inherent geometric asymmetry.

In terms of lift, the NEURALFOIL predictions align well with wind tunnel measurements and 2D CFD predictions up to
 515 approximately $\alpha = 13^\circ$. Beyond this range, however, NEURALFOIL overpredicts lift and delayed stall. For drag, between $\alpha = -5^\circ$ and 10° , the NEURALFOIL and Breukels' predictions exhibit similar trends to those of CFD simulations and wind tunnel measurements, but are off in magnitude. At $\alpha > 20^\circ$, the C_d predictions of NEURALFOIL and the CFD approach the flat-plate wind tunnel measurement, in slope and magnitude.

Among all numerical approaches, 2D CFD simulations exhibit the closest agreement with wind-tunnel measurements.
 520 Within the linear regime, from approximately $\alpha = -1^\circ$ to $\alpha = 10^\circ$, the average percentage errors are 4% and 16% for lift



and drag, respectively. The largest discrepancies occur outside the linear regime, in the negative-lift regime and in the prediction of the stall angle, where 2D CFD indicates a slightly delayed stall onset.

The largest discrepancies among the model predictions arise in the moment coefficient, for which wind-tunnel measurements were unavailable for both the LEI airfoil and the flat plate. Breukels' model yields the greatest deviation from all other approaches. From $\alpha = -3^\circ$ to 3° or so, the CFD results closely follow the flat-plate prediction for C_m . Beginning around $\alpha = 3^\circ$, the CFD predicted C_m diverges from the flat-plate trend and instead flattens, maintaining an almost constant negative value from $\alpha = 5^\circ$ to $\alpha = 12^\circ$. Beyond this point, a sharp decrease in C_m is observed, coinciding with the onset of stall. NEURALFOIL is unable to capture this behaviour, and also deviates strongly with negative angles of attack.

5.3 VSM convergence

The VSM permits arbitrary spanwise panel distributions; for instance, the area between existing strut locations may be divided into equal parts, arranged with a uniform distribution, or spaced according to a cosine-based scheme—commonly used in LL models to concentrate panels near the tips (Phillips and Snyder, 2000). However, for the V3 kite, the cosine distribution proved ineffective and failed to converge when the number of panels n_p exceeded 50, whereas a uniform panel distribution yielded the most robust and reliable convergence as n_p increased.

Within this manuscript, the simulations were considered converged when the metric $\delta_\Gamma < 1 \times 10^{-6}$, and a relaxation factor of $f_{\text{relax}} = 0.01$ was employed to ensure numerical stability.

Figure 12 demonstrates the convergence of aerodynamic coefficients, by showing the percentage error relative to the $n_p = 150$ case, for $\alpha = 5^\circ$, 10° , and 15° . The $n_p = 150$ case was selected as the endpoint because the VSM often failed to converge for larger values of n_p . The results were computed using airfoil data obtained from CFD simulations fitted with PCHIP, and the used V3 kite airfoils are shown in Fig. A2 in App. A.

The convergence analysis demonstrated that convergence deteriorated with increasing α , with markedly less smooth trends at $\alpha = 16^\circ$, consistent with VSM's post-stall behaviour, discussed in Sect. 5.4 and 5.6. Because the solution converged with increasing n_p , the largest panel count, $n_p = 150$, was adopted throughout the remainder of the paper.

5.4 VSM sensitivity to airfoil aerodynamic input

To place the VSM results with different airfoil inputs in context, wind tunnel measurements and accompanying confidence interval (CI) (Poland et al., 2025b) and 3D RANS CFD simulations (Viré et al., 2022) are plotted in Fig. 13, all at a $Re = 5 \times 10^5$, except for the 3D CFD simulations, which are at $Re = 1 \times 10^6$. The 3D CFD simulations demonstrated that both the inclusion of struts and the difference in Reynolds number between $Re = 1.0 \times 10^6$ (with struts) and $Re = 5.0 \times 10^5$ (without struts) had a negligible effect on the integral forces (Viré et al., 2022). The plotted 3D CFD results differ from those presented in (Viré et al., 2022), as they were corrected for a geometric offset of $\Delta\alpha = 1.02^\circ$; further details are provided in the appendix of the companion paper (Poland et al., 2025b).

The VSM results, generated with 2D RANS CFD PCHIP-fitted data, differ slightly from the geometry used in the wind tunnel and 3D CFD, as struts are omitted and differences between the profiles' pressure sides emerge near the tips, an artefact

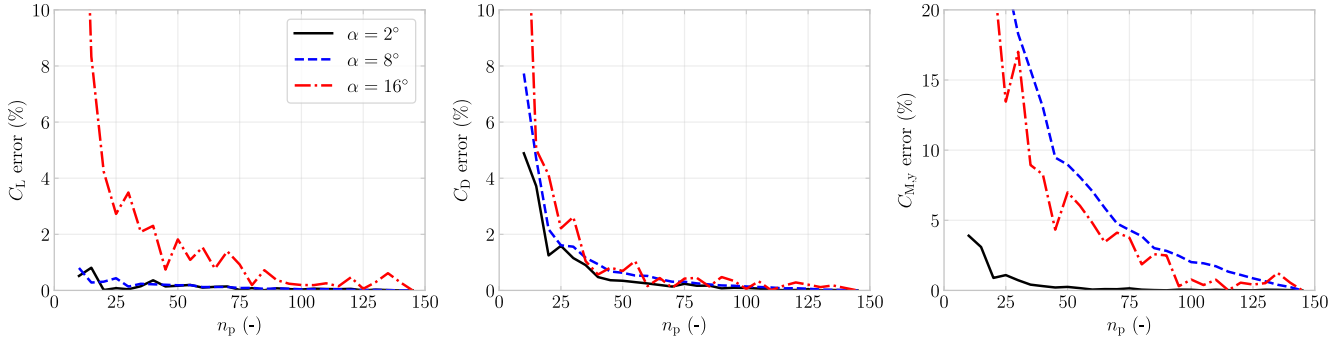


Figure 12. Convergence analysis of the VSM for C_L , C_D , and $C_{M,y}$ at $\alpha = 2^\circ$, 8° , and 16° . The error relative to the reference case with $n_p = 150$ is shown.

of relying on the parametrisation scheme and an automatic meshing script; see Fig. A2 in App. A. The VSM results, on the other hand, rely on NEURALFOIL and do use the geometries with struts. The pitching moment $C_{M,y}$ was defined with respect to the tow point, defined as the location where the bridle lines converge beneath the wing, corresponding to the attachment point of the tether or kite control unit in AWE systems. The tow point of the V3 kite is located at $x = 1.16$ m, $y = 0$ m, and $z = -11$ m, relative to the mid-span LE point. The results are presented in Fig. 13.

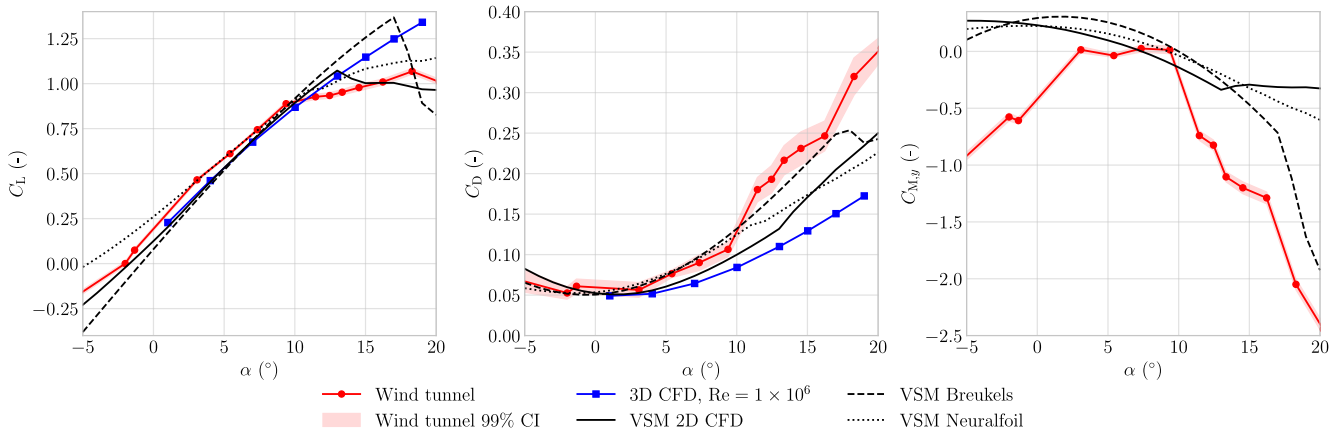


Figure 13. The C_L , C_D and $C_{M,y}$ are plotted over an α , for $\beta = 0^\circ$, for varying VSM simulations, wind tunnel measurements and CFD simulations (Viré et al., 2020; Poland et al., 2025b).

The V3 kite operates at approximately $\alpha \approx 1^\circ$ during reel-in and $\alpha \approx 8^\circ$ during reel-out (Cayon et al., 2025b), placing the nominal operating conditions largely within the near-linear portion of the polar. Accordingly, comparisons are assessed over $\alpha \in [-1, 10]^\circ$ to bracket the operational range and its associated variability.



Within this band, all results shown in Fig. 13 exhibited a consistent linear increase in lift, with the wind tunnel measurements forming the exception with a change in slope around $\alpha = 9^\circ$. At negative α , the VSM results based on 2D CFD data aligned most closely with the measurements. At higher α , where LL models are known to be inaccurate, the VSM 2D CFD predictions surprisingly agreed more closely with the measurements than the 3D CFD data. In drag, the sensitivity of the VSM predictions to the airfoil-level inputs was also evident, where the VSM 2D CFD case—the only one without struts—yielded the lowest drag. Considering both lift and drag, the VSM with 2D CFD input reproduces the measurements more closely than the 3D CFD predictions. Averaged over $\alpha \in [-1, 10]^\circ$, the respective mean absolute errors are 9% for lift and 13% for drag.

The sensitivity of the VSM predictions is most evident in the pitching-moment coefficient $C_{M,y}$, for which no 3D CFD data were available. The VSM results deviated from the measured trend at negative α , and became less negative at higher angles. Within the mentioned α -band, all simulations predicted a continually decreasing $C_{M,y}$, whereas the measurements showed a nearly constant and near-zero $C_{M,y}$.

Overall, it is concluded that the VSM predicted the most consistent trends when using 2D CFD-derived aerodynamic input, primarily because the associated lift and drag polars capture stall behaviour more accurately.

5.5 Rigid-body stability derivatives

Rigid-body stability derivatives were obtained by perturbing the apparent velocity angles and the body rates about a trimmed baseline and evaluating the resulting changes in aerodynamic force and moment coefficients. Angle derivatives with respect to the angle of attack α and sideslip β were reported per radian, whereas rate derivatives with respect to the body rates p , q , and r (roll, pitch, and yaw) were non-dimensionalised to hat-rates using

$$\hat{p} = \frac{pb}{2V}, \quad \hat{q} = \frac{qc_{MAC}}{2V}, \quad \hat{r} = \frac{rb}{2V}, \quad (38)$$

where $c_{MAC} = S/b = 2.346$ m represents the mean aerodynamic chord with projected surface area $S = 19.413$ m² and projected span $b = 8.274$ m. Sensitivity $\partial C/d\xi$ was then approximated using a central finite-difference scheme,

$$\frac{\partial C}{d\xi} \approx \frac{C(\xi + \Delta\xi) - C(\xi - \Delta\xi)}{2\Delta\xi}, \quad (39)$$

with perturbation steps $\Delta\alpha = \Delta\beta = 0.005$ rad and $\Delta p = \Delta q = \Delta r = 0.1$ rads⁻¹.

The perturbation steps were applied around the baseline trim angle, the angle at which $C_{M,y} = 0$ and $dC_{M,y}/d\alpha < 0$, further discussed in Sect. 6. The trim-angle was found at $\alpha_{trim} = 5.906^\circ$ with $\partial C_{M,y}/\partial\alpha = -2.932$ rad⁻¹, indicating local pitch stability. Moments were computed about the tow-point, i.e., the junction where the bridle lines connect beneath the wing, as this represents the physical point about which the kite rotates. The moments are also defined around the tow point.

The resulting derivatives are reported in the aircraft reference frame in Table 8, and represent instantaneous rigid-body stability characteristics and do not capture unsteady aerodynamic effects nor the influence of deformation on the dynamic response. Since deformation was not included, control effects are likewise absent, as the kite wing relies on deformation for actuation. Despite this limitation, the aerodynamically derived stability derivatives still provide insight into the kite's intrinsic



stability characteristics, particularly given the scarcity of comparable data in the literature and the reference-model status of the V3 kite.

Table 8. Computed rigid-body stability derivatives at the trim angle $\alpha_{\text{trim}} = 5.906^\circ$. All quantities are expressed in the aircraft reference frame, where the x -axis is defined positive from the TE to the LE, the y -axis is positive towards the right wing, and the z -axis is positive downward, forming a right-handed coordinate system consistent with standard aerodynamic force and moment sign conventions.

| | ∂C_x | ∂C_y | ∂C_z | $\partial C_{M,x}$ | $\partial C_{M,y}$ | $\partial C_{M,z}$ | Units |
|--------------------|----------------|----------------|----------------|--------------------|--------------------|--------------------|-----------------------|
| $d/\partial\alpha$ | 0.8757 | -0.0000 | -4.1394 | -0.0000 | -2.9318 | 0.0000 | (rad^{-1}) |
| $d/\partial\beta$ | 0.0000 | -1.1794 | -0.0000 | -3.1077 | -0.0000 | 0.3718 | (rad^{-1}) |
| $d/d\hat{p}$ | -0.0000 | 1.8755 | 0.0000 | 5.0072 | 0.0000 | -0.6062 | (-) |
| $d/d\hat{q}$ | -1.1620 | -0.0000 | -3.1664 | -0.0000 | 4.5868 | -0.0000 | (-) |
| $d/d\hat{r}$ | 0.0000 | 0.0205 | 0.0000 | 0.0149 | -0.0000 | 0.1184 | (-) |

595 The signs of the static derivatives— $\partial C_{M,x}/\partial\beta < 0$, $\partial C_{M,y}/\partial\alpha < 0$, and $\partial C_{M,z}/\partial\beta > 0$ —indicated static stability in roll, pitch, and yaw, respectively (Etkin and Reid, 1996). The positive rate derivatives indicate a lack of aerodynamic damping, implying that the configuration is dynamically unstable and would require active control. To resolve the detailed nature of the unstable motion, a full modal analysis would be needed.

5.6 Best practices and limitations

600 VSM, like other LL methods, is sensitive to implementation details, and inconsistent force evaluation can lead to non-physical performance improvements when such models are embedded in optimisation loops. For this reason, the present work has prioritised internal consistency and documented limitations over incremental extensions whose theoretical implications are not fully validated.

605 Examples of excluded incremental extensions include accelerating convergence by initialising the solver with a previously converged circulation distribution. This strategy was omitted because the solution exhibited sensitivity to the initial condition, particularly in the vicinity of stall.

610 Extensions proposed for swept and sideslip configurations were explored but not adopted. The first concerned a sweep-consistent kinematic projection, in which the sectional kinematics were evaluated in the plane normal to the local spanwise direction when coupling the three-dimensional induced velocity to two-dimensional polars, rather than in the global projection plane used in the present VSM formulation; this modification produced only modest changes in the predicted loads. The second involved a modified near-wake treatment, in which the trailing vorticity was initialised locally perpendicular to the lifting line before aligning with the far-wake direction (Goates and Hunsaker, 2021), instead of being directly aligned with the free stream. This modification reduced the predicted lift of the V3 kite by nearly 40%, and was therefore not retained.

615 At high angles of attack, convergence issues may arise when the lift curve becomes non-bijective, such that multiple values of α correspond to the same C_l , particularly in post-stall regimes (Anderson et al., 1980; Chattot, 2004; Mukherjee and



Gopalarathnam, 2006; Hunsaker, 2007; Gallay and Laurendeau, 2015; Dias, 2016; Simonet et al., 2024). Similar discontinuities were observed for the V3 kite in post-stall. To address potential spanwise discontinuities, a simple smoothing algorithm was implemented to damp sharp local gradients in the circulation field during iteration. However, no consistent results were obtained, as the smoothing effectiveness varied with both the number of panels and the geometry. It was therefore decided to omit the proposed algorithm. The model of Simonet et al. (2024) was also tested, but it likewise did not yield consistent results and was therefore excluded.

Discrepancies in drag, most pronounced when comparing numerical results to wind-tunnel measurements (Poland et al., 2025b), may arise from several sources. One notable factor is the absence of a spanwise viscous drag contribution in the baseline model. A correction for this effect, proposed by Gaunaa et al. (2024), accounts for spanwise flow by decomposing the local velocity vector into spanwise and perpendicular components. The correction was omitted from the current VSM implementation due to its empirical nature and limited impact, as it increased drag by approximately 1%.

To aid convergence, smooth sectional polars are recommended. Computational cost can be optimised by using fewer panels, or switching from the open-source Python version to the open-source Julia version, which is about 30 to 50 times faster, and runs in approximately 3 ms with 36 panels and in 25 ms with 150 panels on a 12th Gen Intel® Core™ i7-1265U CPU. The 3D RANS CFD simulations required 19394 s of CPU time (Viré et al., 2022), indicating a speed-up on the order of 10^6 , although the processor specifications for the 3D RANS CFD computations were not documented.

6 Aerodynamic design considerations

The aerodynamic design of kites presents distinct challenges relative to conventional aircraft, stemming fundamentally from their reliance on structural tension for flight integrity and from differences in centre of rotation. Kites are uniquely susceptible to two contrasting stall phenomena: front stall, which generally occurs at low, negative angles of attack, and back stall, which manifests at high, positive angles of attack.

A front stall is often an irrecoverable failure mode. Once the kite initiates a nose-down motion, it is driven into negative angles of attack, where it produces minimal or negative lift. As the aerodynamic loading vanishes, line tension drops, and the tensile structure collapses, rendering the kite into an uncontrollable mass of fabric

In contrast, a back stall usually allows for recovery. During the pitching-back motion, the kite typically retains part of its line tension and thus much of its shape. Control authority can often be restored by depowering, which effectively reduces the angle of attack and stops the stall. When the pitching-back motion is asymmetric, or when depowering is applied too late or insufficiently, the kite often rotates naturally such that its heaviest component—the LE—moves downward first. As the kite accelerates downward, the magnitude of the apparent wind velocity increases, which reduces the effective angle of attack. Once the angle of attack re-enters the attached-flow regime, the separated shear layer can reattach, thereby restoring aerodynamic loading. The resulting renewed line tension re-establishes control authority before ground impact, often with sufficient time to steer the kite and keep it airborne.



In-flight, bridled soft-wing kites naturally align themselves until the net aerodynamic force and the tether attached to the tow-point become parallel, at which point the moment arm vanishes and $C_{M,y} = 0$ (Cayon et al., 2025a). This equilibrium defines the trim angle of attack, α_t , which remains nearly constant because the tow point offers negligible rotational resistance. For a fixed bridle geometry, this equilibrium occurs at a single inflow angle, as corroborated experimentally for two kites, including the V3 kite (Cayon et al., 2025b). The angle changes primarily during the transition phases, because powering and depowering alter the front–rear bridle length ratio, which shifts the effective tow-point location, and thereby modifies the pitching-moment balance that sets α_t .

For AWE systems, the design objective is to maximise the system’s C_L^3/C_D^2 (Loyd, 1980) at the trim angle while maintaining sufficient stability margins to prevent front stall, which requires careful coordination between the wing’s aerodynamic characteristics and the bridle configuration. This section, therefore, presents parametric studies to investigate the effects of airfoil shape in Sect. 6.1, wing planform geometry in Sect. 6.2, and tow-point location in Sect. 6.3. Gravitational contributions are neglected in this analysis, which is considered a reasonable assumption given the low weight of soft kites relative to aerodynamic forces (Cayon et al., 2025a, b). Although aero-structural coupling and unsteady effects are not included, the results provide valuable insight into aerodynamic trends and design trade-offs and should be interpreted within the context of these limitations.

6.1 Effect of airfoil shape variation

To quantify the sensitivity of kite aerodynamic loads to airfoil geometry, the ML model was deployed to systematically vary the geometric parameters, κ , η , t , δ , and λ . The resulting airfoil polars were subsequently used as input for the VSM to evaluate the kite aerodynamic loads. All the airfoil slices, shown in App. A, were uniformly varied by the same percentage relative to the V3 kite reference, while ensuring that all parameter values, shown in Table 3, remained within the bounds used for ML model training. As the V3 kite had a reflex angle of $\delta = 0^\circ$, percentage-based variation was not feasible; therefore, each profile was modified instead by an equal absolute value. The resulting variations are plotted in Fig. 14, with the exception of λ , which, within the parameter bounds used for training the ML model, had the least visible profile change.

The parameter study revealed that the effect on aerodynamic forces is more pronounced than the effect on the pitching moment. It furthermore showed that trends in 2D and 3D aerodynamic performance are not always aligned. For example, while the 2D ratio C_L^3/C_D^2 exhibits a clear peak near $\alpha = 6^\circ$, the C_L^3/C_D^2 gradually increases beyond this angle. Likewise, variations in t affected C_m differently depending on α ; the 2D case exhibited a near constant trend at 10° angle of attack, whereas the corresponding impact on the 3D C_M showed a more uniform, decreasing trend across the investigated range.

For AWE, the aerodynamic design objective is to maximise the system ratio C_L^3/C_D^2 , evaluated at the corresponding trim angle. Compared to the V3 kite, the results indicate that an optimal design would have smaller values of κ , larger values of η , smaller values of t , and a small δ , although for the latter, the opposite holds for $\alpha > 8^\circ$.

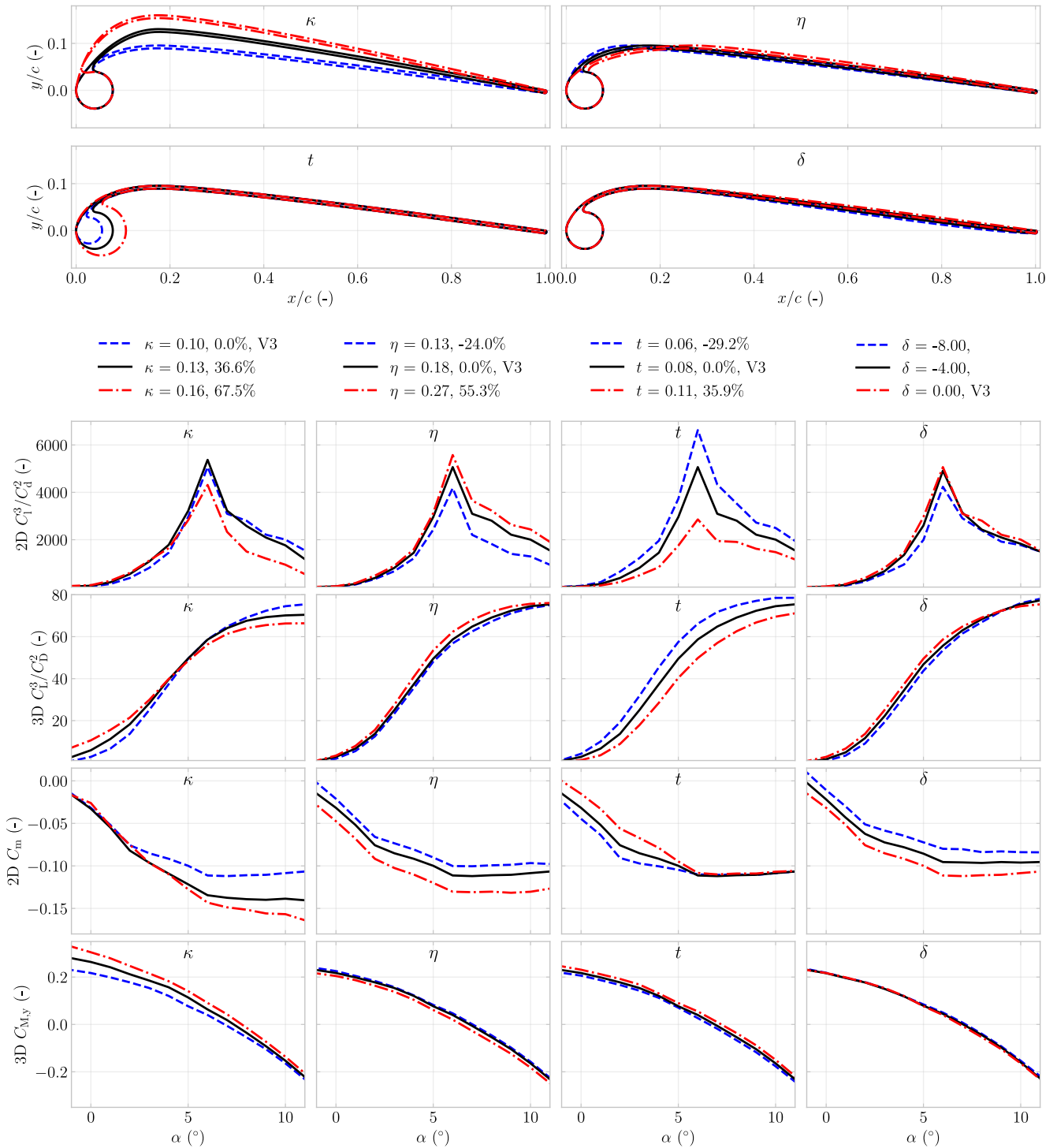


Figure 14. Effect of changing the profile shape on the aerodynamic performance and pitching moment of the airfoil and wing.

6.2 Effect of planform variations

680 The effect of varying the wing planform geometry was analysed by simulating three distinct planforms. A cubic Bézier curve was fitted to the quarter-chord line of the V3 kite wing using four control points (P_1 , P_2 , P_3 , and P_4) that preserved the end-point positions at tip and root, as illustrated in Fig. 15. Two shape parameters, namely the distances from P_1 to P_2 and from P_3 to P_4 , were employed to capture arc fullness and tip curvature. These distances were initially obtained by nonlinear least-squares minimisation of the total point-to-curve distance between measured quarter-chord points. The anhedral angle ϕ_{an} , also shown in Fig. 15, was defined as the angle between the line from P_1 to P_2 and the line from P_1 to P_4 .

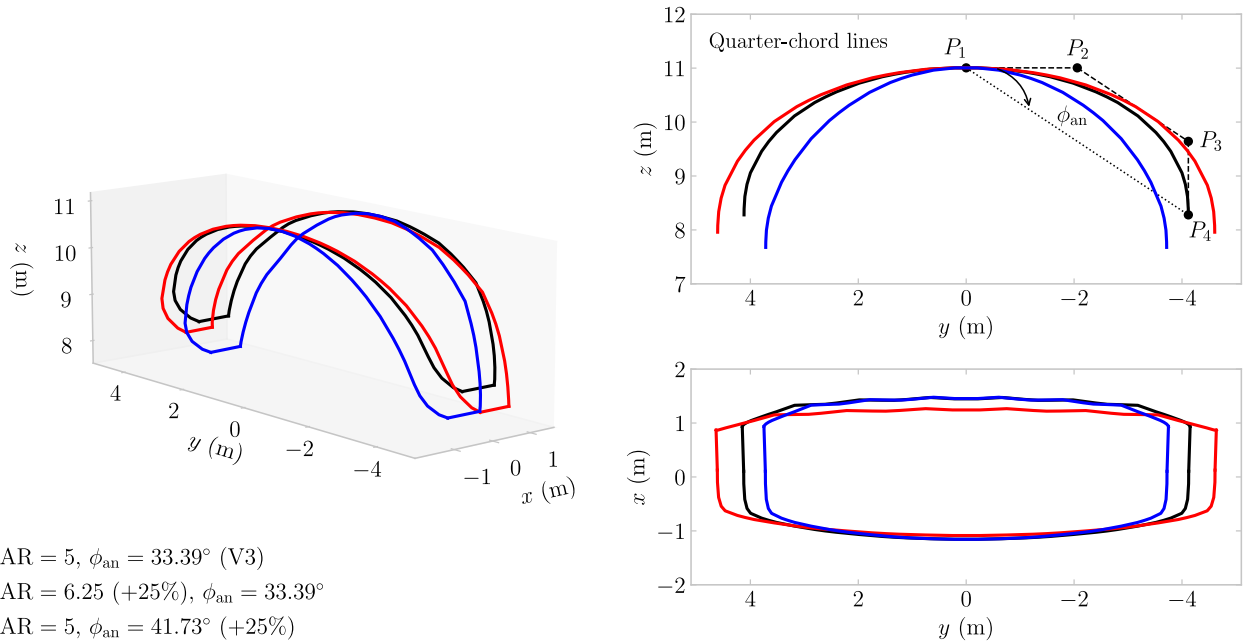


Figure 15. Effect of changing the V3 kite's aspect ratio and ϕ_{an} , from its base properties, while maintaining the same flat surface area.

685

When reconstructing the V3 using cubic Bézier curves, an aspect ratio of $AR = 5$ was found, with AR defined as

$$AR = \frac{b^2}{S}, \quad (40)$$

where $b = 11$ m denotes the flat wingspan, not identical to the projected wingspan, measured as the quarter-chord arc length in the (y, z) -plane when laid out flat.

690 A second planform with the same non-dimensional arc shape, but a 25% larger aspect ratio, was generated by keeping the shape parameters fixed and scaling span and chord. A third planform was produced by increasing the anhedral angle by 25% to $\phi_{an} = 41.73^\circ$. The flattened surface areas of the reference model and enlarged AR planform were nearly identical, where a reduction of less than 0.5% was observed for the planform with enlarged ϕ_{an} .



The aerodynamic effects are presented for both α and β sweeps in Fig. 16. To generate the β -sweep results, the trim angles were calculated: for the baseline configuration, $\alpha_t = 5.47^\circ$; for the AR-scaled configuration, $\alpha_t = 5.28^\circ$; and for the ϕ_{an} -scaled configuration, $\alpha_t = 5.84^\circ$. The maximum difference of 0.6° was not considered substantial in view of the applied shape changes.

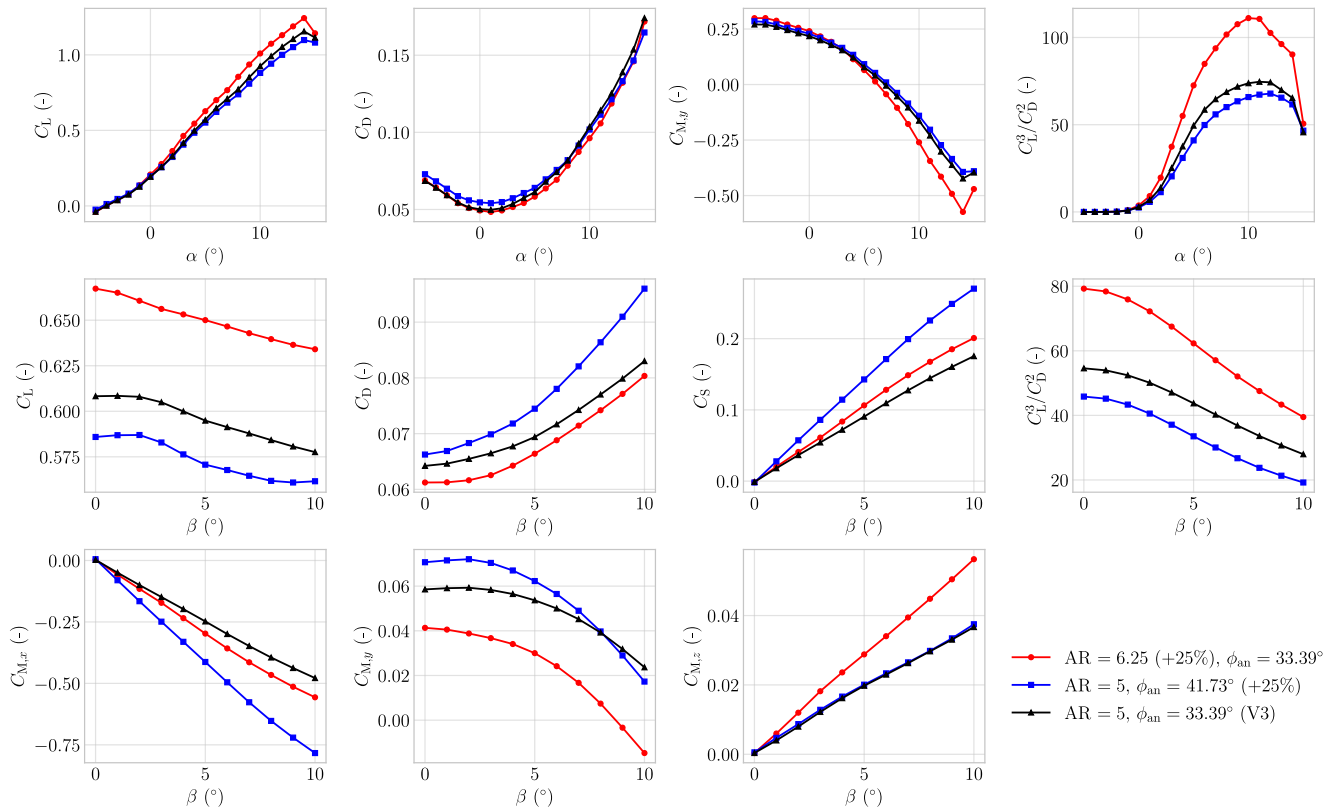


Figure 16. Effect of changing the V3 kite, from its baseline, is shown by plotting the force and moment coefficients over an α and β sweep, the latter using the trim-angle for each respective configuration.

Increasing the aspect ratio AR, in line with classical aircraft aerodynamic theory, resulted in higher C_L^3/C_D^2 values. This was accompanied by a more positive yaw moment derivative $\partial C_{M,z}/\partial\beta$. From this, one could conclude that a kite with a larger AR would generate a greater restoring yaw moment in response to an offset in β , thereby enhancing yaw static stability.

Increasing the anhedral angle ϕ_{an} reduced C_L^3/C_D^2 . In addition, the lateral-directional coefficients exhibited stronger coupling: the side-force coefficient C_S increased in magnitude for a given β , indicative of enhanced turning capability.

The results demonstrated a fundamental trade-off in kite design. Increasing AR yielded a higher lift-to-drag ratio, whereas increasing the ϕ_{an} lowered C_L^3/C_D^2 but enhanced the turning ability.



705 6.3 Effect of tow point location

The sensitivity of the kite to variations in tow-point position was analysed by displacing its location in the x - and z -directions, as illustrated in Fig. 17, which also includes a V3 kite mid-span slice showing the LEI airfoil at the design distance, spanning precisely the figure x -limits. For each tow-point configuration, the trim angle α_t and its corresponding C_L^3/C_D^2 ratio were determined using the VSM. Since the VSM tends to lose accuracy in post-stall conditions, the analysis was restricted to the
710 range $\alpha \in [-3^\circ, 13^\circ]$.

The figures include a grey-shaded region indicating the region where $\partial C_{M,y}/\partial\alpha < 0$, i.e., where the kite is not pitch statically stable and no physically meaningful trim angle can be found. Additionally, the centre of gravity (CG) and the range of centre-of-pressure (CP) positions corresponding to the obtained trim angles were calculated and plotted.

The results indicate that the trim angle, α_t , is more sensitive to variations in x than in z . The same trend is observed for
715 C_L^3/C_D^2 , $\partial C_{M,y}/\partial\alpha$, and $\partial C_{M,z}/\partial\beta$. The largest trim angles α_t , corresponding to the largest values of C_L^3/C_D^2 , occur when the tow point is positioned aft of the CP. However, positioning the tow point excessively close to the TE should be avoided, as it may lead to static pitch instability. More restrictive is the yawing-moment derivative, $\partial C_{M,z}/\partial\beta$, which shows that parts of the region yielding the highest C_L^3/C_D^2 coincide with $\partial C_{M,z}/\partial\beta < 0$, implying static instability in yaw.

The $\partial C_{M,x}/\partial\beta$ is the only parameter that is more sensitive to variations in z than in x , and it indicates static roll stability at
720 the design tow-point location. The results show that raising the tow point can eliminate the restoring roll moment. This implies the existence of a boundary in tow-point height at which the effective roll moment arm about the wing changes sign, rendering the kite statically unstable in roll. Since the CG lies above this boundary, placing the tow point at the CG location would lead to static roll instability. Such behaviour is consistent with expectations for an anhedral wing in conventional aircraft (Etkin and Reid, 1996), and it underscores a key distinction: kites that rotate about a sufficiently low tow point require anhedral for roll
725 stability, whereas aircraft that rotate about the CG require dihedral.

The tow-point variation analysis shows that to avoid static pitch and yaw instability, the tow point must be placed sufficiently far forward, which becomes more restrictive at higher z values. The stability gains of placing the tow-point forward come at the cost of a reduced trim angle and, thereby, a lower aerodynamic performance.

7 Conclusion

730 A computationally efficient aerodynamic framework for soft-wing kite design was developed by coupling a vortex step method (VSM) with CFD-informed airfoil polars obtained from more than 10^5 RANS CFD simulations. The resulting novel RANS-trained machine-learning surrogate predicts lift, drag, and moment coefficients for parametrised LEI airfoils within the trained design space; three models were trained at $Re = 1 \times 10^6$, 5×10^6 , and 2×10^7 , achieving $R^2 > 0.98$ on held-out test data.

735 Within the operational, near-linear incidence band $\alpha \in [-1, 10]^\circ$, selected to bracket the reported reel-in and reel-out angles of attack of the V3 kite, the underlying 2D CFD data agreed with wind-tunnel measurements with mean errors of 4% in lift and 16% in drag. When these polars were used as VSM inputs, three-dimensional lift and drag predictions matched wind-tunnel results within this band on average by 9% and 13%, respectively, reproducing measured lift and drag trends more consistently

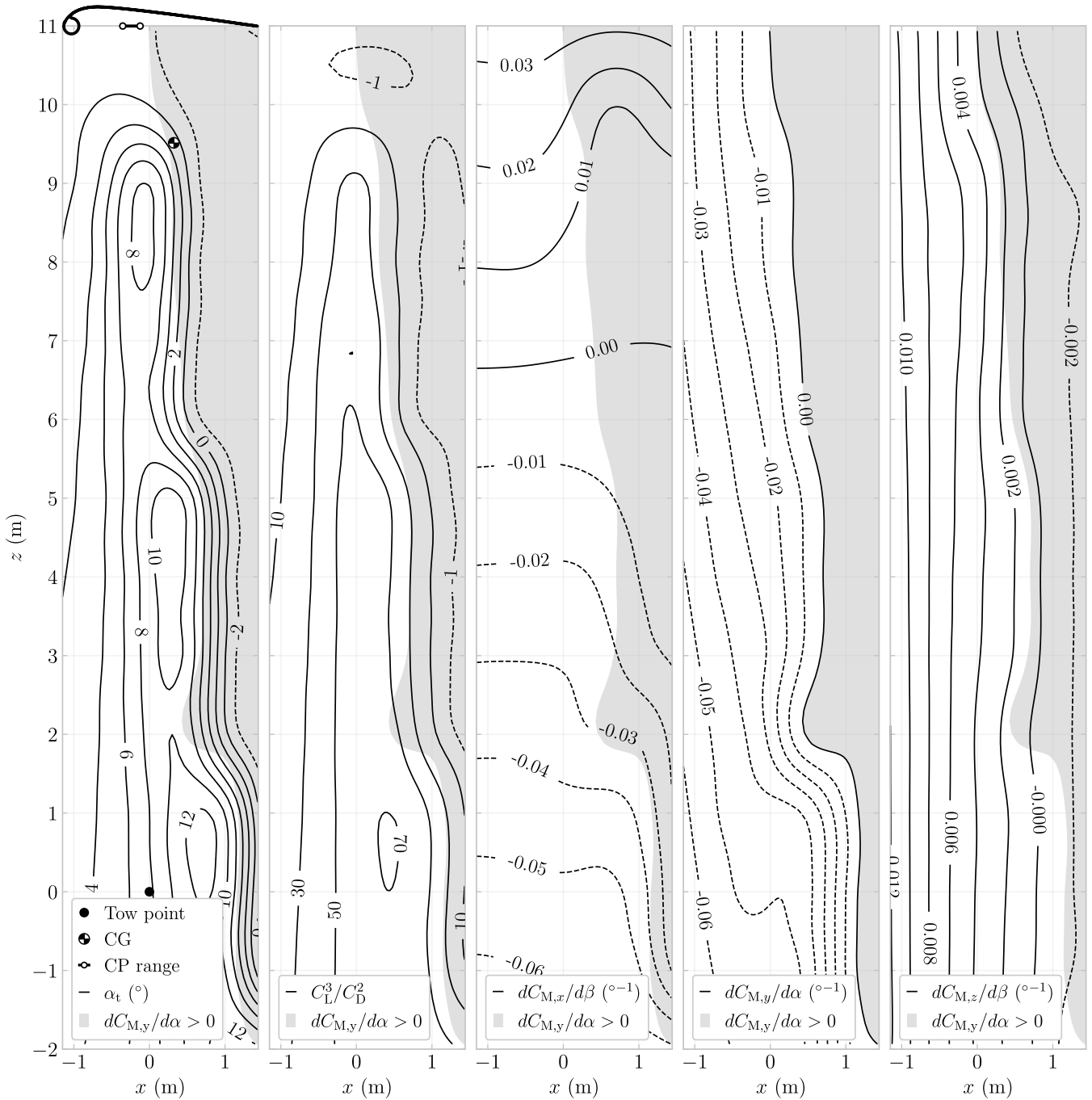


Figure 17. Effect of tow-point displacement on the V3 kite aerodynamic characteristics. The left panel shows the mid-span airfoil, the CP range, and the CG. All plots show isolines of varying parameters. The left plot shows the trim angle α_t as a function of tow-point location in the x - and z -directions. The other plots, show the isolines for C_L^3/C_D^2 , $dC_{M,x}/d\beta$, $dC_{M,y}/d\alpha$ and $dC_{M,z}/d\beta$.



than the available 3D RANS CFD results. The latter required 19394 s of CPU time, whereas the present framework evaluated the $n_p = 150$ case in approximately 25 ms on the stated CPU, corresponding to an estimated speed-up of $\mathcal{O}(10^6)$ for the compared configurations, subject to differences in hardware, parallelisation, and included preprocessing. This computational efficiency facilitates optimisation, aero-structural coupling, and real-time control applications.

Rigid-body analysis yielded a novel numerically derived set of static stability derivatives for the TU Delft V3 reference kite. The configuration was found to be statically stable in roll, pitch, and yaw for the examined trim condition, whereas the computed rate derivatives indicate limited aerodynamic damping within the present quasi-steady aerodynamic model, suggesting that active control is likely required. A dedicated modal analysis, including unsteady aerodynamics, is required to characterise the associated dynamic modes. Accordingly, within the present quasi-steady, rigid-geometry analysis, the roll-stability mechanism reverses: anhedral is stabilising for kites rotating around the tow-point, whereas dihedral is stabilising for aircraft rotating about the centre of gravity.

Parametric analysis revealed that configurations maximising aerodynamic efficiency, expressed as C_L^3/C_D^2 , do not coincide with those improving static stability margins (e.g. via $\partial C_{M,y}/\partial\alpha$ and $\partial C_{M,z}/\partial\beta$), indicating a multi-objective design problem.

The framework provides a validated and computationally efficient basis for conceptual and preliminary kite design. Future work should integrate aero-structural coupling to resolve wing deformation and its feedback on aerodynamic loading, for example, by updating spanwise sectional polars in response to the local deformed airfoil geometry and operating point. In addition, optimisation studies would benefit from incorporating variations in bridle geometry and tow-point positioning to quantify their coupled influence on aerodynamic performance and stability.

Appendix A: Profile distribution

Geometric differences exist between the various simulation approaches. To illustrate these differences, Fig. A1 shows a spanwise slice taken at 25% of the chord length of the V3 kite at $\alpha = 6^\circ$, plotted for half of the span. As shown in Fig. A2, nineteen chordwise slices are defined, ranging from ‘1’ at the mid-span to ‘19’ at the tip. The three simulation techniques differ in the airfoil geometry across these profiles, illustrated in Fig. A2.

The 3D RANS CFD analysis conducted by Viré et al. (2020) employed a smoothed geometry, which incorporated substantial edge fillets downstream of the LE. The 2D RANS CFD simulations, undertaken to facilitate direct comparison with the 3D RANS CFD results, similarly included large edge fillets but did not account for the struts. The ML model, by comparison, was trained on 2D CFD datasets generated from geometries designed to approximate the physical configuration as closely as possible. Consequently, it cannot predict geometries with such large edge fillets; hence, only fillets of significantly reduced dimension are present relative to the other simulated geometries.

As the tip region was approached, the 2D slice intersected the LE tube at an increasingly shallow angle; that is, less perpendicular and more parallel to the tube axis. This progression increased the disparity between the respective geometries, most apparent for profiles ‘18’ and ‘19’ in Fig. A2. As the trained ML model focuses on the LEI airfoil shape, it does not capture these changes.

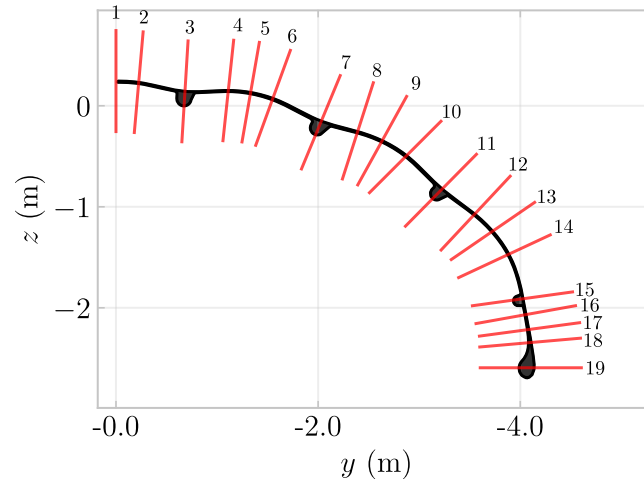


Figure A1. Slice distribution along a representative spanwise section of the V3 kite at $\alpha = 6^\circ$, evaluated at 25% chord. The figure is selected for illustrative purposes and does not correspond to the exact physical position.

Appendix B: Evaluating force direction

Li et al. (2022) revisited the chordwise placement of the control point in LL-type formulations by embedding unsteady two-dimensional thin airfoil theory into a generalised three-dimensional framework. Building on the classical thin airfoil solution, they showed that the quasi-steady lift magnitude is formally linked to the effective angle of attack evaluated at the three-quarter-chord point, consistent with the Kutta condition and with the location where the no-through-flow boundary condition is enforced in Weissinger-type discretisations. In contrast, the direction of the aerodynamic force is governed by the local flow angle at the quarter-chord point, where the bound vortex resides.

Li et al. (2022) validated their correction against blade-resolved RANS CFD simulations of wind turbine rotors with finite thickness and viscous effects, and demonstrated improved agreement for coned configurations. For a 15° coned rotor, the theoretically consistent two-point approach reduced power prediction errors by 8–10% relative to simplified one-point implementations, resulting in noticeably closer agreement with CFD.

To assess the applicability of the correction, derived from unsteady thin-airfoil theory, to highly swept, anhedral kite wings, VSM simulations were performed for the TU Delft V3 LEI kite and a ram-air kite using two alternative implementations: (i) a standard three-quarter-chord evaluation for both force magnitude and direction ($3/4c$), and (ii) Li's suggested approach in which the magnitude is evaluated at three-quarter-chord while the direction is evaluated at quarter-chord ($1/4c$). The validation dataset comprised wind tunnel measurements for both geometries, supplemented by 3D RANS CFD for the V3 LEI kite.

Figure B1 shows that, although both implementations predict C_L accurately and are in close agreement with the measurements and CFD, the $1/4c$ method systematically underpredicts C_D relative to the reference data. As a result, the predicted C_L/C_D is consistently overestimated. Both kites exhibit similar trends, with the discrepancy being most pronounced for the

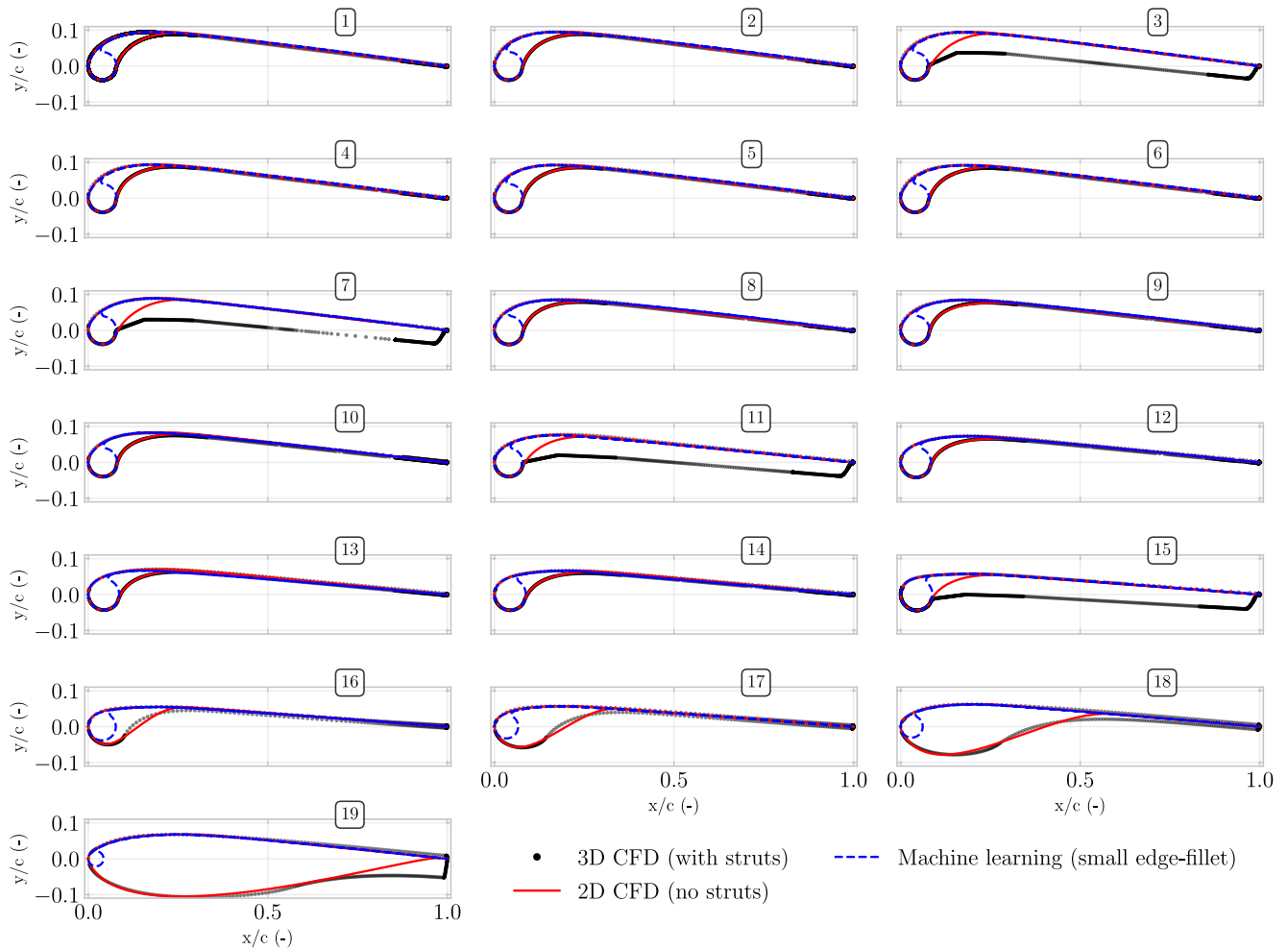


Figure A2. Profiles used for simulations, and their differences.

790 V3 LEI kite. In contrast to the wind turbine results of Li et al. (2022), the standard 3/4c implementation yields better overall
 agreement with the experimental and numerical reference data, particularly for the key metric C_L/C_D .

The reason why the correction degrades, rather than improves, the drag prediction accuracy is not yet understood. Conse-
 quently, it cannot be concluded that the method proposed by Li et al. (2022) is fundamentally incorrect. Instead, based on the
 present validation results, it is inferred that, for the investigated geometries, the standard 3/4c implementation provides the
 795 closest agreement with the measurements and is therefore adopted throughout this work.

Li et al. (2022) additionally proposed a single evaluation point pitch-rate correction for unsteady cases. But as evaluating
 this correction requires validation data with known pitch histories, which is currently unavailable for these configurations, the
 present comparison is limited to steady conditions.

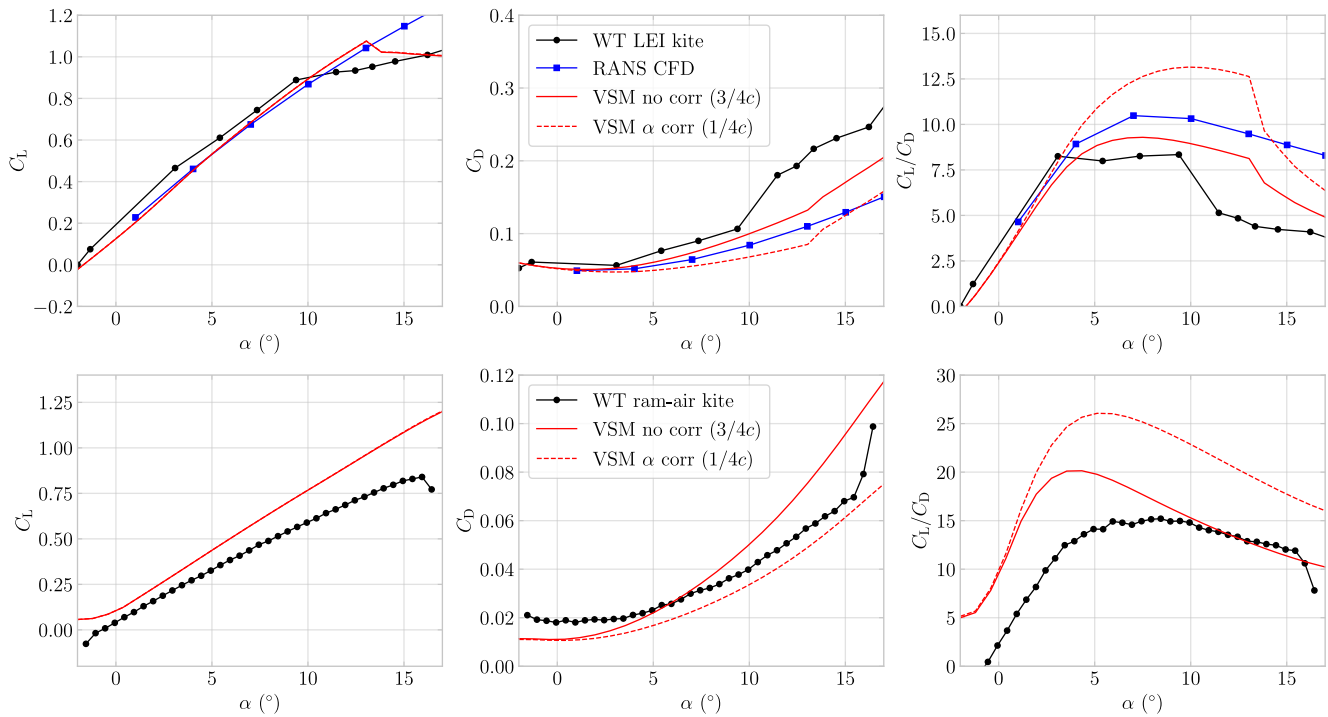


Figure B1. Effect of varying the force-direction evaluation point, shown using VSM simulations performed at the Reynolds numbers of their respective wind tunnel (WT) measurements, which are included for comparison. Plotted are C_L , C_D , and C_L/C_D against α for the TU Delft V3 LEI kite and the ram-air kite (Poland et al., 2025b; Belloc, 2015).

Appendix C: Assuming fully turbulent flow

800 In 2019, Folkersma et al. (2019) showed with 2D RANS CFD that explicitly modelling boundary layer transition affected the aerodynamic predictions for $Re < 2 \times 10^7$ under a low freestream turbulence intensity of approximately 2%. This finding motivated the subsequent use of natural-transition models in 3D RANS CFD studies of the V3 kite (Viré et al., 2020, 2022). Recent field measurements of the Kitepower B.V. V9 kite system, however, reported turbulence intensities between 5% and 805 environment than that assumed by Folkersma et al. (2019). Elevated freestream turbulence intensities are known to promote earlier boundary layer transition, both in terms of lower critical Reynolds numbers (Fransson et al., 2005; Zhang et al., 2020) and reduced critical roughness heights (Jain et al., 2024). Taken together, these observations suggested that the operational flow regime of the industrial kite system was closer to fully turbulent conditions than to the low-disturbance environment assessed in the original 2D study.



810 In addition to the atmospheric turbulence, the full-scale kite geometry introduced significant surface roughness elements not considered by Folkersma et al. (2019), which might trigger transition. On the suction side, the canopy was attached to the leading-edge (LE) tube by a zigzag-patterned stitching seam located on top of a forward step running along the span, while the pressure side featured a closing seam where the canopy wrapped around the LE tube. The obstacle height associated with the LE seam, representing the combined effect of the stitching and the step, was measured as $k = 0.6$ mm (Masure, 2025). In a 2D
815 LEI wind tunnel experiment a zigzag roughness height of 0.3 mm was found to already be sufficient to trip the boundary layer at $Re = 5 \times 10^5$ (van Lith, 2025). This is consistent with classical roughness-induced transition theory. The onset of transition by a roughness element of height k is commonly characterised as,

$$k = \frac{Re_{k,crit} \nu}{U_k}, \quad (C1)$$

where ν represents dynamic viscosity, U_k represents the local velocity at the roughness height (Braslow and Knox, 1958).
820 One finds that the roughness scales inversely with the velocity. In other words, the faster the flow is, and thereby the higher the Reynolds number, the smaller the roughness height needs to be. Given that 0.3 mm was found sufficient at $Re = 5 \times 10^5$, 0.6 mm was deemed sufficient at $Re = 3 \times 10^6$, the approximately averaged Reynolds number encountered during the V3 flight (Cayon et al., 2025b).

For the pressure side, van Lith (2025) reported that the pressure side flow close to the LE tube should be characterised
825 by a different Reynolds number. Using the tube diameter as a characteristic length, an effective Reynolds number was found that is roughly one order of magnitude smaller than on the suction side. Masure (2025) found the closing seam height to be approximately ten times larger than the suction-side zigzag seam, the direct opposite. In terms of the roughness Reynolds number, these two effects approximately compensated each other, suggesting that the pressure-side seam also operated above the critical roughness threshold.

830 Although detailed boundary layer measurements on the pressure side were not available, and thus a definitive experimental confirmation could not be provided, the combined evidence of (i) substantially higher atmospheric turbulence levels than in previous low-disturbance CFD studies, (ii) supercritical stitching seams on at least the suction side, and likely also on the pressure side, and (iii) the trend towards higher Reynolds numbers with continued industrial upscaling, provided the basis for assuming fully turbulent boundary layers in the presented 2D CFD simulations. This modelling choice was considered more
835 representative of the operational flow conditions than not modelling the suction- and pressure-side seams and letting the flow transition naturally over a smooth surface.

Appendix D: Machine learning model

Building the machine learning (ML) model involved several steps, illustrated in Fig. D1. In the blue boxes on the top-left, the data creation steps are shown. This involved defining a parameter grid, running 2D RANS CFD simulations, and splitting the
840 data into training and test sets. Both datasets were preprocessed, and outliers were removed as explained in Sect. 4.

In the purple block, the model setup is illustrated. Building the ML model began with standardising the filtered training datasets using a standard scaler to ensure consistent weighting of all input parameters. Multiple regression algorithms were

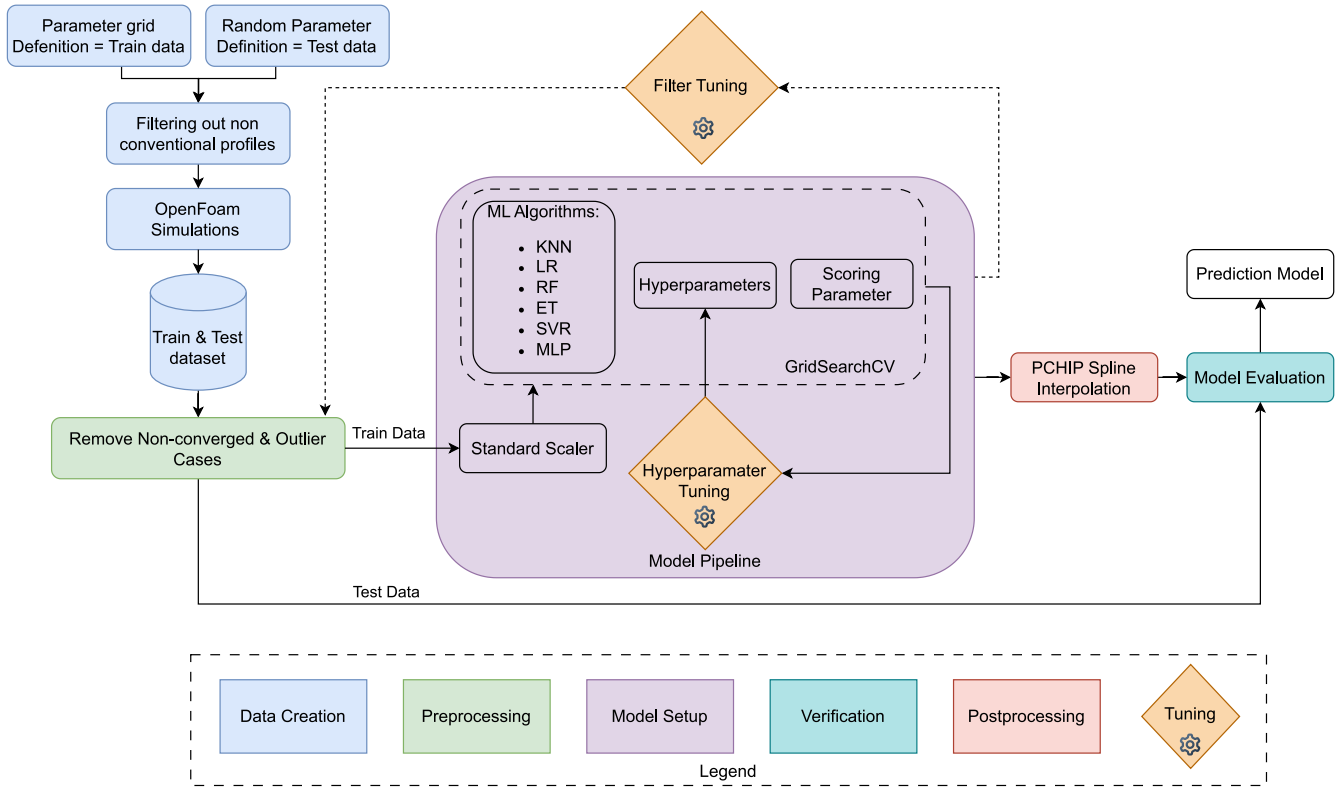


Figure D1. ML model setup flowchart, from data preprocessing to model evaluation.

then evaluated using their default settings (Pedregosa et al., 2011), with the selected models chosen for their strong baseline performance reported by (Pandala, 2021). Linear regression (LR) was also included for reference. The hyperparameters of the selected algorithms were subsequently optimised using a grid-search procedure with k -fold cross-validation, using the coefficient of determination R^2 as the scoring metric. The dataset size was sufficient to allow reliable training-validation splits while still retaining a large and representative test set.

After hyperparameter tuning, the final models were evaluated on the independent test set. To ensure smooth behaviour between sampled angles of attack, the model outputs were post-processed using a piecewise cubic Hermite interpolating polynomial (PCHIP) spline.



Table D1. Overview of ML models, hyperparameters, and R^2 values.

| ML model | Hyperparameters | R^2 (-) |
|---------------------------------|---|-----------|
| K-nearest neighbours (KNN) | number of neighbours= 8 | 0.945 |
| Linear regression (LR) | – | 0.617 |
| Random forest (RF) | n-estimators=130, max-features=sqrt, min-samples-split=2 | 0.993 |
| Extra trees (ERT) | n-estimators=130, max-depth=None, max-features=log2, min-samples-split=2 | 0.991 |
| Support vector regression (SVR) | kernel=rbf, C=1, epsilon=0.1, gamma=scale | 0.737 |
| Multi-layer perceptron (MLP) | hidden-layer-sizes=100, activation=tanh | 0.941 |

Code and data availability. The geometric mesh of the TU Delft V3 kite is available on Zenodo from <https://doi.org/10.5281/zenodo.15316036> and through https://awegroup.github.io/TUDELFT_V3_KITE/docs/datasets.html, which also contains more information and other datasets. The code for generating the diagrams in this paper is available on Zenodo <https://doi.org/10.5281/zenodo.18351808> or directly on GitHub https://github.com/jellepoland/WES_aero_sim_for_kite_design. The data supporting this paper, needed to run the code, is available through Zenodo from <https://doi.org/10.5281/zenodo.18351331>. The code relies on version 2.1.2 of the vortex-step method, available on GitHub: <https://github.com/ocayon/Vortex-Step-Method>. The geometry, wind tunnel results, and polars used in App. B for the Belloc (2015) case are available at <https://github.com/fairaero/Belloc-validation-data> (Accessed on 16/02/2026).

Author contributions. JAWP compiled the original manuscript and performed the analysis shown in the results. KRGM performed the CFD and ML analysis, assisted in creating figures, and reviewed the manuscript. OC co-developed the latest version of the VSM, provided input to Chapter 6, and reviewed the manuscript several times. RS supervised the project and reviewed the manuscript.

Competing interests. At least one of the (co-)authors is a member of the editorial board of Wind Energy Science.

Acknowledgements. We would like to thank <https://fair.aero/> for open-sourcing the rigid paraglider data. We acknowledge the use of OpenAI's ChatGPT and Grammarly for assistance in refining the writing style of this manuscript.

Financial support. This research has been supported by the Nederlandse Organisatie voor Wetenschappelijk Onderzoek (NWO) under grant number 17628. This work has been partially supported by the MERIDIONAL project, which receives funding from the European Union's Horizon Europe Programme under the grant agreement No. 101084216.



References

- Anderson, J., Corda, S., and Wie, D. V.: Numerical lifting line theory applied to drooped leading-edge wings below and above stall, *Journal of Aircraft*, 17, 898–904, <https://doi.org/10.2514/3.44690>, 1980.
- 870 Barnes, J. P.: Semi-Empirical Vortex Step Method for the Lift and Induced Drag Loading of 2D or 3D Wings, in: Proceedings of the 1997 World Aviation Congress, Anaheim, CA, USA, <https://doi.org/10.2514/6.1997-5559>, 1997.
- Batchelor, G.: An Introduction to Fluid Dynamics, Cambridge University Press, <https://doi.org/10.1017/CBO9780511800955>, 1967.
- Belloc, H.: Wind Tunnel Investigation of a Rigid Paraglider Reference Wing, *Journal of Aircraft*, 52, 703–708, <https://doi.org/10.2514/1.C032513>, 2015.
- 875 Bhagwat, M. J. and Leishman, J. G.: Generalized Viscous Vortex Model for Application to Free-Vortex Wake and Aeroacoustic Calculations, in: Proceedings of the 58th Annual Forum and Technology Display of the American Helicopter Society International, https://www.researchgate.net/publication/255470975_Generalized_viscous_vortex_model_for_application_to_free-vortex_wake_and_aeroacoustic_calculations, accessed on 16/02/2026, 2002.
- Bosch, A., Schmehl, R., Tiso, P., and Rixen, D.: Dynamic nonlinear aeroelastic model of a kite for power generation, *Journal of Guidance, Control and Dynamics*, 37, 1426–1436, <https://doi.org/10.2514/1.G000545>, 2014.
- 880 Branlard, E., Brownstein, I., Strom, B., Jonkman, J., Dana, S., and Baring-Gould, E.: A multipurpose lifting-line flow solver for arbitrary wind energy concepts, *Wind Energy Science*, 7, 455–467, <https://doi.org/10.5194/wes-7-455-2022>, 2022.
- Braslow, A. and Knox, E.: Simplified method for determining critical height of distributed roughness particles for boundary-layer transition, Tech. Rep. TN 4363, NACA, <https://ntrs.nasa.gov/citations/19930085292>, accessed on 16/02/2026, 1958.
- 885 Breukels, J.: An Engineering Methodology for Kite Design, Ph.D. thesis, Delft University of Technology, <http://resolver.tudelft.nl/uuid:cdece38a-1f13-47cc-b277-ed64fdda7cdf>, 2011.
- Breukels, J., Schmehl, R., and Ockels, W.: Aeroelastic Simulation of Flexible Membrane Wings based on Multibody System Dynamics, in: Airborne Wind Energy, edited by Ahrens, U., Diehl, M., and Schmehl, R., Green Energy and Technology, chap. 16, pp. 287–305, Springer, Berlin Heidelberg, https://doi.org/10.1007/978-3-642-39965-7_16, 2013.
- 890 Brown, G.: Parafoil Steady Turn Response to Control Input, in: Aerospace Design Conference, <https://doi.org/10.2514/6.1993-1241>, 1993.
- Candade, A. A., Ranneberg, M., and Schmehl, R.: Aero-structural Design of Composite Wings for Airborne Wind Energy Applications, *Journal of Physics: Conference Series*, 1618, 032 016, <https://doi.org/10.1088/1742-6596/1618/3/032016>, 2020.
- Castro-Fernández, I., Sánchez-Arriaga, G., and García-Villalba, M.: A review of the aerodynamics of airborne wind energy systems, *Progress in Aerospace Sciences*, 161, 101 157, <https://doi.org/10.1016/j.paerosci.2025.101157>, 2026.
- 895 Cayon, O., Gaunaa, M., and Schmehl, R.: Fast Aero-Structural Model of a Leading-Edge Inflatable Kite, *Energies*, 16, 3061, <https://doi.org/10.3390/en16073061>, 2023.
- Cayon, O., van Deursen, V., and Schmehl, R.: Translational Dynamics of Bridled Kites: A Reduced-Order Model in the Course Reference Frame, *Wind Energy Science Discussions* [preprint], <https://doi.org/10.5194/wes-2025-205>, 2025a.
- Cayon, O., Watson, S., and Schmehl, R.: Kite as a Sensor: Wind and State Estimation in Tethered Flying Systems, *Wind Energy Science*, 10, 2161–2188, <https://doi.org/10.5194/wes-10-2161-2025>, 2025b.
- 900 Chattot, J.-J.: Analysis and design of wings and wing/winglet combinations at low speeds, in: Proceedings of the 42nd AIAA Aerospace Sciences Meeting and Exhibit, Reno, NV, USA, <https://doi.org/10.2514/6.2004-220>, 2004.



- Cone, C. D. J.: The Theory of Induced Lift and Minimum Induced Drag of Nonplanar Lifting Systems, Tech. Rep. NASA TR R-139, NASA, <https://ntrs.nasa.gov/citations/19630006412>, accessed on 16/02/2026, 1962.
- 905 Damiani, R., Wendt, F., Jonkman, J., and Sicard, J.: A Vortex Step Method for Nonlinear Airfoil Polar Data as Implemented in KiteAeroDyn, in: Proceedings of the AIAA Scitech 2019 Forum, San Diego, CA, USA, <https://doi.org/10.2514/6.2019-0804>, 2019.
- Deaves, M.: An Investigation of the Non-Linear 3D Flow Effects Relevant for Leading Edge Inflatable Kites, Master's thesis, Delft University of Technology, <https://resolver.tudelft.nl/uuid:ccb56154-0b70-4a41-8223-24b0f8d145c5>, accessed on 16/02/2026, 2015.
- Dekking, F., Kraaikamp, C., Lopuhaä, H., and Meester, L.: A Modern Introduction to Probability and Statistics: Understanding Why and
910 How, Springer, London, 1 edn., <https://doi.org/10.1007/1-84628-168-7>, 2005.
- Den Boer, R.: Low Speed Aerodynamic Characteristics of a Two-Dimensional Sail Wing with Adjustable Slack of the Sail, Tech. Rep. LR-307, Technische Hogeschool Delft, Luchtvaart- en Ruimtevaarttechniek, <https://resolver.tudelft.nl/uuid:18ae2cc6-434e-49c8-9296-d3fa450850a5>, accessed on 16/02/2026, 1980.
- Dias, J. N.: Nonlinear lifting-line algorithm for unsteady and post-stall conditions, in: Proceedings of the 34th AIAA Applied Aerodynamics
915 Conference, pp. 1–11, Washington, DC, USA, <https://doi.org/10.2514/6.2016-4164>, 2016.
- Drela, M.: XFOIL Subsonic Airfoil Development, <https://web.mit.edu/drela/Public/web/xfoil/>, accessed on 16/02/2026, 2013.
- Duport, C.: Modeling with consideration of the fluid-structure interaction of the behavior under load of a kite for auxiliary traction of ships, Ph.D. thesis, University of Bretagne, <https://theses.hal.science/tel-02383312>, 2018.
- Duport, C., Leroux, J.-B., Roncin, K., Jochum, C., and Parlier, Y.: Benchmarking of a 3D non-linear lifting line method against 3D RANSE
920 simulations, *La Houille Blanche*, 105, 70–73, <https://doi.org/10.1051/lhb/2019029>, 2019.
- Durston, D. A.: LinAir: A multi-element discrete vortex Weissinger aerodynamic prediction method, NASA Technical Memorandum NASA-TM-108786, NASA Ames Research Center, Moffett Field, CA, USA, <https://ntrs.nasa.gov/citations/19940019084>, accessed 16 February 2026, 1993.
- Elfert, C., Göhlich, D., and Schmehl, R.: Measurement of the turning behaviour of tethered membrane wings using automated flight manoeuvres, *Wind Energy Science*, 9, 2261–2282, <https://doi.org/10.5194/wes-9-2261-2024>, 2024.
925
- Etkin, B. and Reid, L. D.: Dynamics of Flight: Stability and Control, John Wiley & Sons, 3rd edn., ISBN 978-0-471-03418-8, 1996.
- Ferrari, R.: Towards the adoption of a Vortex Step Method for the aerodynamic evaluations in fixed-wing AWESs flight simulators, Master's thesis, Politecnico di Milano, <https://hdl.handle.net/10589/203860>, accessed on 16/02/2026, 2023.
- Ferziger, J. H., Perić, M., and Street, R. L.: Computational Methods for Fluid Dynamics, Springer Nature Switzerland AG, Cham, Switzerland, 4 edn., <https://doi.org/10.1007/978-3-319-99693-6>, 2020.
930
- Folkersma, M., Schmehl, R., and Viré, A.: Boundary layer transition modeling on leading edge inflatable kite airfoils, *Wind Energy*, 22, 908–921, <https://doi.org/10.1002/we.2329>, 2019.
- Folkersma, M., Schmehl, R., and Viré, A.: Steady-State Aeroelasticity of a Ram-Air Wing for Airborne Wind Energy Applications, *Journal of Physics: Conference Series*, 1618, 032 018, <https://doi.org/10.1088/1742-6596/1618/3/032018>, 2020.
- 935 Folkersma, M. A. M.: Aeroelasticity of Membrane Kites, Ph.D. thesis, Delft University of Technology, <https://doi.org/10.4233/uuid:eae39f5a-49bc-438b-948f-b6ab51208068>, 2022.
- Fransson, J. H. M., Matsubara, M., and Alfredsson, P. H.: Transition induced by free-stream turbulence, *Journal of Fluid Mechanics*, 527, 1–25, <https://doi.org/10.1017/S0022112004002770>, 2005.
- Fritz, E. K.: Swept Away: Numerical and Experimental Investigations into Swept Wind Turbine Blades, Ph.D. thesis, Delft University of
940 Technology, <https://doi.org/10.4233/uuid:55415991-053c-4c74-b31a-3db8724bfab7>, 2024.



- Gallay, S. and Laurendeau, E.: Nonlinear generalized lifting-line coupling algorithms for pre/poststall flows, *AIAA Journal*, 53, 1784–1792, <https://doi.org/10.2514/1.J053530>, 2015.
- Garrel, A. V.: Development of a Wind Turbine Aero-Module for FOCUS, Tech. rep., Energy Research Centre of the Netherlands (ECN), <https://publications.ecn.nl/ECN-C--03-079>, accessed on 16/02/2026, 2003.
- 945 Gaunaa, M., Li, Y., Pirrung, G., Kallesøe, B. S., and Madsen, H. A.: A correction model for the effect of spanwise flow on the viscous force contribution in BEM and Lifting Line methods, *Journal of Physics: Conference Series*, 2767, 022 068, <https://doi.org/10.1088/1742-6596/2767/2/022068>, 2024.
- Gaunaa, M. et al.: A Computationally Efficient Method for Determining the Aerodynamic Performance of Kites for Wind Energy Applications, in: EWEA Annual Event 2011, European Wind Energy Association (EWEA), https://backend.orbit.dtu.dk/ws/portalfiles/portal/6241674/Gaunaa_poster_EWEA2011presentation%5B1%5D.pdf, accessed on 16/02/2026, 2011.
- 950 Glauert, H.: *The Elements of Aerofoil and Airscrew Theory*, Cambridge [Eng.]: The University Press, 1 edn., <https://archive.org/details/dli.ernet.19686/>, accessed on 16/02/2026, 1926.
- Goates, C. and Hunsaker, D.: Practical Implementation of a General Numerical Lifting-Line Method, in: *AIAA Scitech 2021 Forum*, <https://doi.org/10.2514/6.2021-0118>, accessed on 16/02/2026, 2021.
- 955 Hummel, J., Göhlich, D., and Schmehl, R.: Automatic measurement and characterization of the dynamic properties of tethered membrane wings, *Wind Energy Science*, 4, 41–55, <https://doi.org/10.5194/wes-4-41-2019>, 2019.
- Hunsaker, D.: Post stall behavior of a lifting line algorithm, Salt Lake City, UT, USA, https://digitalcommons.usu.edu/mae_facpub/103/, 2007.
- Jain, I., Katiyar, S., and Sarkar, S.: Influence of Varying Freestream Turbulence on Flow Transition Over Distributed Surface Roughness, in: *Proceedings of the ASME Turbo Expo 2024: Turbomachinery Technical Conference and Exposition, GT2024*, p. V12CT32A018, ASME, <https://doi.org/10.1115/GT2024-124283>, 2024.
- Jonkman, J.: Google/Makani Energy Kite Modeling; Cooperative Research and Development Final Report, Tech. Rep. CRD-18-00569 NREL/TP-5000-80635, National Renewable Energy Laboratory, <https://www.nrel.gov/docs/fy21osti/80635.pdf>, accessed on 16/02/2026, 2021.
- 965 Kappel, R. V.: Aerodynamic analysis tool for dynamic leading edge inflated kite models: a nonlinear vortex lattice method, Master's thesis, Delft University of Technology, <https://resolver.tudelft.nl/uuid:385d316b-c997-4a02-b0f3-b30c40fffc32>, accessed on 16/02/2026, 2012.
- Kitepower: Kitepower; Airborne Wind Energy; Plug & Play, Mobile Wind Energy, <https://thekitepower.com/>, accessed on 09-01-2025, 2025.
- Kutta, M. W.: Auftriebskräfte in strömenden Flüssigkeiten, *Illustrierte Aeronautische Mitteilungen*, 6, 133, 1902.
- Leloup, R., Roncin, K., Bles, G., Leroux, J. B., Jochum, C., and Parlier, Y.: Estimation of the lift-to-drag ratio using the lifting line method: Application to a leading edge inflatable kite, in: *Airborne Wind Energy*, edited by Ahrens, U., Schmehl, R., and Diehl, M., chap. 19, pp. 339–355, Springer, https://doi.org/10.1007/978-3-642-39965-7_19, 2013.
- 970 Leuthold, R.: Multiple-Wake Vortex Lattice Method for Membrane Wing Kites, Master's thesis, Delft University of Technology, <http://resolver.tudelft.nl/uuid:4c2f34c2-d465-491a-aa64-d991978fedf4>, accessed on 16/02/2026, 2015.
- Li, A., Gaunaa, M., Pirrung, G., Forsting, A., and Horcas, S.: How Should the Lift and Drag Forces Be Calculated from 2-D Airfoil Data for Dihedral or Coned Wind Turbine Blades?, *Wind Energy Science*, 7, 1341–1365, <https://doi.org/10.5194/wes-7-1341-2022>, 2022.
- Lolies, T., Gourdain, N., Charlotte, M., and Goldsmith, B.: Numerical Methods for Efficient Fluid–Structure Interaction Simulations of Paragliders, *Aerotecnica Missili & Spazio*, 98, 221–229, <https://doi.org/10.1007/s42496-019-00017-2>, 2019.



- Loyd, M. L.: Crosswind kite power (for large-scale wind power production), *Journal of Energy*, 4, 106–111, <https://doi.org/10.2514/3.48021>, 1980.
- 980 Masure, K.: Regression Model of Leading Edge Inflatable Kite Profile Aerodynamics, Master's thesis, Delft University of Technology, <https://resolver.tudelft.nl/uuid:865d59fc-ccff-462e-9bac-e81725f1c0c9>, accessed on 16/02/2026, 2025.
- Menter, F. R.: Two-equation eddy-viscosity turbulence models for engineering applications, *AIAA Journal*, 32, 1598–1605, <https://doi.org/10.2514/3.12149>, 1994.
- Mukherjee, R. and Gopalathnam, A.: Poststall prediction of multiple-lifting-surface configurations using a decambering approach, *Journal of Aircraft*, 43, 660–668, <https://doi.org/10.2514/1.15149>, accessed on 16/02/2026, 2006.
- 985 Mukherjee, R., Gopalathnam, A., and Kim, S.: An Iterative Decambering Approach for Post-Stall Prediction of Wing Characteristics Using Known Section Data, Tech. Rep. AIAA 2003-1097, NASA Langley Research Center, <https://ntrs.nasa.gov/citations/20040085758>, 2003.
- Munk, M.: Airship Theory, Tech. Rep. Technical Report 184 & 191, National Advisory Committee for Aeronautics (NACA), <https://ntrs.nasa.gov/citations/19930091249>, accessed on 16/02/2026, 1923.
- 990 Mutterperl, W.: The Calculation of Span Load Distributions on Swept-Back Wings, Tech. Rep. Technical Note 834, National Advisory Committee for Aeronautics (NACA), Langley Memorial Aeronautical Laboratory, Washington, <https://ntrs.nasa.gov/api/citations/19930081578/downloads/19930081578.pdf>, accessed on 16/02/2026, 1941.
- Oehler, J. and Schmehl, R.: Aerodynamic characterization of a soft kite by in situ flow measurement, *Wind Energy Science*, 4, 1–21, <https://doi.org/10.5194/wes-4-1-2019>, 2019.
- 995 OpenFOAM: OpenFOAM is the free, open source CFD software developed primarily by OpenCFD Ltd since 2004., <https://www.openfoam.com/>, [software] accessed on 16/02/2026, 2025.
- Pandala, S.: lazypredict: Lazy Machine Learning, <https://github.com/shankarpandala/lazypredict>, [software] accessed on 16/02/2026, 2021.
- Pedregosa, F., Varoquaux, G., Gramfort, A., Michel, V., Thirion, B., Grisel, O., Blondel, M., Prettenhofer, P., Weiss, R., Dubourg, V., Vanderplas, J., Passos, A., Cournapeau, D., Brucher, M., Perrot, M., and Duchesnay, E.: Scikit-learn: Machine Learning in Python, *Journal of Machine Learning Research*, 12, 2825–2830, 2011.
- 1000 Phillips, W. F. and Snyder, D. O.: Modern Adaptation of Prandtl's Classic Lifting-Line Theory, *Journal of Aircraft*, 37, 662–670, <https://doi.org/10.2514/2.2649>, 2000.
- Pistoiesi, E.: *Aerodinamica*, Biblioteca dell'Ingegnere, Scienze Propedeutiche, I, Unions Tipografica Editrice Torinese, <https://openlibrary.org/works/OL8269760W/Aerodinamica?edition=key%3A/books/OL6290732M>, accessed on 16/02/2026, 1932.
- 1005 Piszkin, S. T. and Levinsky, E. S.: Nonlinear Lifting Line Theory for Predicting Stalling Instabilities on Wings of Moderate Aspect Ratio, Tech. Rep. AD-A027 645, General Dynamics/Convair, <https://apps.dtic.mil/sti/citations/ADA027645>, accessed on 16/02/2026, 1976.
- Pointwise, F.: Pointwise, <https://www.cfd-technologies.co.uk/fidelity-pointwise/>, [software] accessed on 16/02/2026, 2025.
- Poland, J. A. W., Fritz, E., and Schmehl, R.: Flow Field Analysis Around a Leading-Edge Inflatable Kite Using Stereoscopic PIV and CFD, *Wind Energy Science Discussions* [preprint], <https://doi.org/10.5194/wes-2025-217>, 2025a.
- 1010 Poland, J. A. W., van Spronsen, J., Gaunaa, M., and Schmehl, R.: Wind Tunnel Load Measurements of a Leading-Edge Inflatable Kite Rigid Scale Model, *Wind Energy Science Discussions* [preprint], <https://doi.org/10.5194/wes-2025-77>, in review, 2025b.
- Prandtl, L.: Tragflügeltheorie. I. Mitteilung, *Nachrichten von der Gesellschaft der Wissenschaften zu Göttingen, Mathematisch-Physikalische Klasse*, 1918, 451–477, <http://eudml.org/doc/59036>, accessed on 16/02/2026, 1918.
- Ranneberg, M.: Direct Wing Design and Inverse Airfoil Identification with the Nonlinear Weissinger Method, <https://doi.org/10.48550/arXiv.1501.04983>, 2015.
- 1015



- Sharpe, P.: NeuralFoil: An airfoil aerodynamics analysis tool using physics-informed machine learning, <https://github.com/peterdsharpe/NeuralFoil>, [software] accessed on 16/02/2026, 2023.
- Sharpe, P. D.: Accelerating Practical Engineering Design Optimization with Computational Graph Transformations, Ph.D. thesis, Massachusetts Institute of Technology, <https://hdl.handle.net/1721.1/157809>, 2024.
- 1020 Simonet, T., Roncin, K., Faure, T., and Daridon, L.: An Efficient 3D Non-Linear Lifting-Line Method with Correction for Post-Stall Regime [preprint], <https://doi.org/10.21203/rs.3.rs-3955527/v1>, 2024.
- Sivells, J. C. and Neely, R. H.: Method for Calculating Wing Characteristics by Lifting-Line Theory Using Nonlinear Section Lift Data, Tech. Rep. Report 865, National Advisory Committee for Aeronautics (NACA), <https://ntrs.nasa.gov/citations/19930091938>, accessed on 16/02/2026, 1947.
- 1025 Tani, I.: A Simple Method of Calculating the Induced Velocity of a Monoplane Wing, Bulletin of the Aeronautical Research Institute, Tokyo Imperial University, 9, 64–76, <https://jaxa.repo.nii.ac.jp/records/35482>, accessed on 16/02/2026, 1934.
- Thekens, P.: An integrated aero-structural model for ram-air kite simulations: with application to airborne wind energy, Ph.D. thesis, Delft University of Technology, <https://doi.org/10.4233/uuid:16e90401-62fc-4bc3-bf04-7a8c7bb0e2ee>, 2022.
- van Dorn, N. H. and DeYoung, J.: A Comparison of Three Theoretical Methods of Calculating Span Load Distribution on Swept Wings, Tech. Rep. NACA-TN-1476, National Advisory Committee for Aeronautics (NACA), <https://ntrs.nasa.gov/citations/19930082478>, accessed on 16/02/2026, 1947.
- 1030 van Lith, T. L. B.: Aerodynamic Analysis of a 2D Rigid LEI Airfoil: An Experimental and Numerical Study, Master's thesis, Delft University of Technology, <https://resolver.tudelft.nl/uuid:53c595f1-2beb-4cc3-853d-f3a51a116690>, accessed on 16/02/2026, 2025.
- Viré, A., Demkowicz, P., Folkersma, M., Roullier, A., and Schmehl, R.: Reynolds-averaged Navier-Stokes simulations of the flow past a leading edge inflatable wing for airborne wind energy applications, Journal of Physics: Conference Series, 1618, 032007, <https://doi.org/10.1088/1742-6596/1618/3/032007>, 2020.
- 1035 Viré, A., Lebesque, G., Folkersma, M., and Schmehl, R.: Effect of Chordwise Struts and Misaligned Flow on the Aerodynamic Performance of a Leading-Edge Inflatable Wing, Energies, 15, 1450, <https://doi.org/10.3390/en15041450>, 2022.
- Watchorn, P.: Aerodynamic Load Modelling for Leading Edge Inflatable Kites, Master's thesis, Delft University of Technology, <https://resolver.tudelft.nl/uuid:42f611a2-ef79-4540-a43c-0ea827700388>, accessed on 16/02/2026, 2023.
- 1040 Weissinger, J.: The Lift Distribution of Swept-Back Wings, Tech. Rep. Technical Memorandum 1120, National Advisory Committee for Aeronautics (NACA), Washington, <https://ntrs.nasa.gov/api/citations/20030064148/downloads/20030064148.pdf>, translation of Forschungsbericht Nr. 1553: Über die Auftriebsverteilung von Pfeilflügeln, 1947.
- Wick, B. H.: Study of the Subsonic Forces and Moments on an Inclined Plate of Infinite Span, Technical Note NACA-TN-3221, National Advisory Committee for Aeronautics, Washington, D.C., <https://ntrs.nasa.gov/api/citations/19930084119/downloads/19930084119.pdf>, accessed on 16/02/2026, 1954.
- 1045 Zhang, Y., Zhou, Z., Wang, K., and Li, X.: Aerodynamic Characteristics of Different Airfoils under Varied Turbulence Intensities at Low Reynolds Numbers, Applied Sciences, 10, 1706, <https://doi.org/10.3390/app10051706>, 2020.